UNIVERSITY OF CALIFORNIA, SAN DIEGO

Vibrational and Quantum Yield Studies of Deuterated Tryptophan Radical in Azurin

A thesis submitted in partial satisfaction of the requirements for the degree
Master of Science

in

Chemistry

by

Justine Hwai-Han Liang

Committee in charge:

Professor Judy Kim, Chair
Professor Rommie Amaro
Professor Ulrich Müller

2017

The Thesis of Justine Hwai-Han Liang is approved, and it is acceptable in quality and form for publication on microfilm and electronically:

_____

_____

_____

Chair

University of California, San Diego

2017

TABLE OF CONTENTS

LIST OF ABBREVIATIONS

Derivative Type	**Abbreviation and Other Names**	**Description**
H5NH-Zn^{II}Az48W	Zn^{II}Az48W, or H5-Zn^{II}Az48W, or NH-Zn^{II}Az48W	Fully protiated trp-48 with Zn^{II} metal center
D5NH-Zn^{II}Az48W	D5-Zn^{II}Az48W	Perdeuterated trp-48 (deuterated C-H bonds along indole ring), with Zn^{II} metal center
H5ND-Zn^{II}Az48W	ND-Zn^{II}Az48W	Singly-deuterated trp-48 at N-H moiety, with Zn^{II} metal center
H5NH-apoAz48W	H5-apoAz48W	Fully protiated trp-48 without a metal center
H5NH-Cu^{II}Az48W	H5-Cu^{II}Az48W	Fully protiated trp-48 with a Cu^{II} metal center

LIST OF FIGURES

LIST OF TABLES

ACKNOWLEDGMENTS

First and foremost, I want to thank my advisor, Professor Judy Kim, for giving me the opportunity to do graduate-level research. I had very little research experience during my undergraduate years, devoting most of my time to my classes and volunteering. Even though I had little research experience at the time, Judy was understanding and still gave me a chance, motivating me to pursue a Master's degree in chemistry. I definitely would not be graduating with an M.S. in chemistry without her continuous support and optimism. Her positive attitude, even in the most stressful times, has definitely inspired me. Even though she had to deal with the responsibilities of being Vice Chair of Education and teaching undergraduate classes, Judy still had time to help me with my problems in lab. All in all, I probably will not find another PI as compassionate and genuinely supportive as Professor Kim, and I will continue to be grateful for the opportunities she has given me in the last three years.

I want to thank Professor Mike Tauber and the Tauber group for allowing me to use their lab space and instruments. The photolysis and visible resonance Raman experiments were all done in the Tauber Lab, where I was given the freedom to use the Tauber UV-Vis, the Aminco fluorometer (specifically using the Xe arc lamp), and the Kr/Ar laser. I want to also thank Sam Doyle and Megan Stone for their guidance on using these instruments.

I would not be as experienced as I am now, in spectroscopy and in research, if I did not have the support of the Kim lab members. The current and past members of the Kim lab are the most hardworking, determined, and meticulous individuals. First, I want to thank Ignacio Lopez-Pena who taught me how to be a self-sufficient,

independent researcher; he pushed me to think critically, to solve my own problems, and to clean up after myself. His knowledge and his advice has always miraculously fixed my novice experimental pitfalls. Even though I worked with her for a short period of time, I want to thank Dr. Guipeun Kang for being a great role model; she is an extremely patient individual with an unrelenting smile. Her presence is still in the Kim Lab, as we always say to ourselves "what would Guipeun do" whenever we're in a complex situation. Joel Rivera is also on the azurin project and has helped and motivated me through the years with his innovative ideas and strong work ethic. His creative ways of dealing with lab problems, his positivity, and his patience has definitely inspired me. Furthermore, I want to thank Joel for helping me directly with my Raman and photolysis experiments in the past. DeeAnn Asamoto and Jen Daluz are humble, lighthearted, and kind individuals. We all started at the Kim Lab around the same time, and I'm glad I was able to do research alongside them. They have been a great support system and their kindness and humor has always brightened my day. I also want to thank Ivan Kozachenko, another past member of the Kim Group, for being a great desk neighbor and colleague. His intense focus, work ethic, and determination to finish anything he starts motivated me during my own research endeavors. I would not have completed my thesis work if it weren't for the help of these fellow graduate students of the Kim Lab.

My parents have been incredibly patient with me during the last three years. I was indecisive in my future, mentally running back and forth between continuing onto a doctoral program or continuing to pursue medical school. In the end, they were understanding in my decision to continue onto a doctoral degree in a different program

and field. My parents are the ones that really motivated me to work hard in any aspect of my life. I would not have the dedication and mental willpower to continue onto graduate school if not for their undying support. I strive to succeed in hopes of one day being able to support these loving individuals.

Lastly, I have to acknowledge David Skarbrevik, who drove me to lab every day for the last three years. Besides being a great mode of transportation, David is someone who constantly encouraged and supported me in every decision I made during graduate school. I have to thank him for his positivity and his reassuring words whenever I felt overwhelmed about my research.

These individuals that surrounded me during my graduate years have made positive impacts in several aspects of my life. I matured a lot from my experience in the Kim Lab and I am confident, now, that I can succeed in my next step.

ABSTRACT OF THE THESIS

Vibrational and Quantum Yield Studies of Deuterated Tryptophan Radical in Azurin

by

Justine Hwai-Han Liang

Master of Science in Chemistry

University of California, San Diego, 2017

Professor Judy Kim, Chair

Long-range electron transfer has been observed in several complex biological systems, including photosynthetic complexes to redox enzymes in DNA repair pathways. The efficiency of electron tunneling and hopping through amino acid mediators, including tyrosine and tryptophan, has been reported in the past. In particular, tryptophan residues are redox active and can function as electron transfer

(ET) intermediates through progressive conversion to cation and neutral radical. The current work extends upon the published studies of the tryptophan radical at position 48 of the zinc-substituted protein, azurin (denoted Zn^{II}Az48W) by focusing on the effect of isotopic substitution on electron and protein transfer steps. Two Zn^{II}Az48W isotopologues of trp-48 are studied here: perdeuterated D5- Zn^{II}Az48W and singly-deuterated ND- Zn^{II}Az48W. These isotopologues were characterized by UV- and visible-resonance Raman spectroscopy for both the closed shell and neutral radical forms, respectively. Isotope effects were also observed in the fluorescence and radical quantum yields. The fluorescence and phosphorescence intensities, in the presence and absence of an external electron acceptor, indicate that the triplet state may be involved in the ET and cation radical formation pathways. The quantum yield for formation of D5- Zn^{II}Az48W is consistent with ET from the triplet state. In the case of ND-Zn^{II}Az48W, ET also likely occurs from the triplet state, but there is an additional effect because deprotonation of the heavy deuteron reduces the quantum yield for radical formation by a factor of 0.67 relative to NH- Zn^{II}Az48W. These isotope studies of Trp-48 in azurin help clarify the sequential ET/PT steps for trp-48 in azurin, and provide general insights into this complex biological process.

1 General Introduction

Electron transfer is the simplest form of a chemical reaction, and yet is the basis of the complex processes of energy storage and transduction in all biological systems. It is well established that several types of redox-active moieties are effective mediators in long-range electron transfer (ET). Nature has evolved to allow multistep, long-range ET to occur efficiently via protein-protein interactions, propagating electrons through metal cofactors, organic molecules, or the lesser- known aromatic amino acid carriers. The expected kinetic and energetic barriers that come with charge separation over long distances is logarithmically diminished for electron tunneling[1] and multistep hopping facilitated by intermediates, such as amino acid residues.

The utilization of aromatic amino acid residues as "hopping spots" for long-range ET reactions can be more complicated than a typical metal cofactor because the formation of amino acid radicals involves a proton-coupled ET (PCET) mechanism. Published studies on PCET are extensively devoted to tyrosine-based electron transfer, with its concerted electron- and proton-transfers steps that result in the formation of neutral tyrosine radicals, e.g. in ribonucleotide reductase and photosystem II[2,3,4]. Our goal is to focus on the PCET mechanism of tryptophan, whose electron- and proton-transfer events are generally not considered to be concerted; tryptophan neutral and cation radicals are also observed in complex enzymatic systems, such as DNA photolyase.

Both tryptophan- and tyrosine-mediated electron transfer is observed in a variety of enzymes. In photosystem II, tyrosine-Z mediates electron transfer between P680 and OEC (Oxygen Evolving Complex), subsequently generating molecular

oxygen and protons necessary for initiating ATP synthesis. Tyrosine as a conduit of electron transfer in several enzymatic systems involves a direct hydrogen transfer, where the PCET mechanism is a concerted step of electron ejection and deprotonation, resulting in an energetically favorable formation of a neutral tyrosyl radical. This concerted mechanism bypasses the formation of a high-energy $Tyr\bullet^{+}$ intermediate ($E°=1.45V$ vs NHE[5]). In contrast to the concerted deprotonation reported for tyrosine-mediated ET, tryptophan exhibits a coupled, stepwise ET/PT mechanism that also results in the formation of a stable, neutral Trp• radical. For instance, DNA photolyase incorporates a chain of tryptophan residues that propagates charge transfer from Tyr306 to FADH[6], creating and filling holes from one tryptophan cation radical to another, and lastly generating a neutral tryptophan radical after deprotonation of the cation radical to bulk solvent[6, 7]. The observation of neutral tryptophan radicals in proteins motivates in-depth studies on how the protein environment is able to eliminate high-energy charged intermediates during long-range electron hopping events.

The tryptophan radical has been observed in azurin, a type I cupredoxin metalloprotein naturally found in *Pseudomonas aeruginosa*. This bacterial protein participates in the denitrification cycle, and enables electron shuttling between redox partners, cytochrome c551 and nitrite reductase[8]. Azurin has 128 amino acids that form a globular structure composed of 12 beta sheet strands, 4 alpha helices, loops, and a disulfide bridge (Figure 1.1). It contains one native tryptophan at position 48, with two neighboring tyrosine residues at positions 72 and 108. The copper center is ligated with five amino acids arranged in a specific conformation: His-46, His-117 and

Cys-112 coordinates with the metal and forms a trigonal planar structure, while Met-121 and Gly-45 residues are axial ligands that weakly coordinate to copper. This specific coordination sphere of the copper metal in azurin (Figure 1.2) gives rise to the spectroscopically characterized ligand-to-metal charge transfer (LMCT) band, seen in type I copper proteins, that has an absorption peak at 628 nm (Figure 1.3).

Our group has utilized azurin as a model system to study the tryptophan radical at position 48. When the copper center is exchanged for redox-inactive zinc (coordination sphere shown in Figure 1.2), and the two native tyrosine residues are mutated to phenylalanine, the mutant is called Zn^{II}Az48W. This mutant generates a relatively stable tryptophan radical upon photoexcitation, and in the presence of an electron acceptor. Previous studies on Zn^{II}Az48W have proposed a mechanism of neutral tryptophan radical formation[9], including proposal of a path for trp$\bullet^{+}$ deprotonation from the hydrophobic pocket[10]. The location of the trp-48 residue embedded in the hydrophobic pocket of azurin eliminates the possibility of solvent interaction and, thus, favors the formation of a long-lived neutral trp radical. Our current goal is to further elucidate the mechanism of trp-mediated PCET in azurin with the study of tryptophan isotopologues.

Isotope effects are common tools for monitoring enzyme-substrate activity[11], whether in determining the rate-limiting step of enzyme kinetics or the geometries of substrate bound to enzyme. Notably, kinetic isotope effects (KIEs), defined as a rate ratio kh/kd, can play a large role in investigating PCET exchange[12]. In this study, we utilize the rates of formation of the neutral radical and compare the radical formation kinetics for two types of Zn^{II}Az48W isotopologue derivatives: 1) perdeuterated D5-

Zn^{II}Az48W (full exchange of the five C-H bonds of the trp-48 indole ring to C-D), and 2) singly-deuterated ND- Zn^{II}Az48W, where the exchangeable N1-H proton on the indole ring undergoes H/D exchange to form N1-D on trp-48. Vibrational studies can provide insight into the structures of closed- shell trp-48 and its neutral radical (denoted W48•) upon deuteratation. Paired with their vibrational structures, the radical and fluorescence quantum yields of these isotopologue derivatives will be discussed.

Insight into neutral radical formation in single proteins can bridge the gap from simplified single-protein and electron acceptor models to larger protein-protein electron transfer complexes. We aim to unravel the mechanism of long range, protein mediated ET, where nature has enabled proteins to simultaneously allow electron conduction through long distances while minimizing the energetic costs of charged cation byproducts.

1.2 General Methods of Zn^{II}Az48W Sample Preparation

1.2.1 Az48W Mutant Expression

A modified version of published Azurin expression protocol[13,14] has been pursued in order to express the Az48W mutant (site-directed mutagenesis, transformation to competent cells, and preparation of cell stocks were already completed by previous group members). A generic recipe involving LB (Lysogeny Broth) media was used to express Az48W. All steps for protein expression were carried out under sterile conditions (i.e. autoclaving the media and/or working under the flame). The starter flask was made with 500 mL of LB media and was inoculated with a pipette-tip amount of Az48W frozen cell stock. An ampicillin stock of

100mg/mL was made, and 1 mL of the antibiotic stock was added to the starter flask prior to inoculation. This 500 mL starter bacterial solution was incubated overnight for 12-14 hours (at 37°C). After 12 hours of incubation, 50 mL aliquots of the cloudy starter solution were transferred directly to the larger flasks (6 L capacity). These large flasks each contained 2 L of LB media with 2 mL of the ampicillin stock. The growth of bacteria in the larger flasks was monitored using a UV-Vis spectrometer (Hewlett-Packard 8453). Once the absorbance at 600 nm reached a range from 0.6 to 0.8, 2 mL of 2mM isopropyl β-D-1-thiogalactopyranoside (IPTG) was added to each large flask to initiate protein production. The cells are induced for at least 3 hours, or when the maximum absorption limit was reached (OD600~1.5). The cells were then harvested using a large centrifuge (6000 RPM at 4°C) and washed with 50mM Tris-HCl Buffer pH=7.8. The final pellet of cells was stored in the -80°C freezer until ready to lyse.

1.2.2 Az48W Lysis

The frozen pellet was taken from -80°C and thawed at room temperature (the freeze-thaw cycle aided the cell lysing process). The thawed pellet was resuspended in 40 mL of 20mM KPi buffer (pH 7.2) and mixed with 10mg/mL of lysozyme (Gold Bio) and 500 units of DNAse I. The mixture was then incubated and shaken at 25 - 30°C for 90 minutes. The lysate was then separated from the cell debris through 30-minutes centrifugation. A 1 M sodium acetate buffer of pH 4.5 was used to adjust the pH of the lysate solution to acidic conditions, precipitating out unwanted species; 3 mL of this acetate buffer was needed to precipitate unwanted cell debris. The lysate

was equilibrated in the acidic solution for 30 minutes. After centrifuging (30 minutes at 17000 RPM, 4°C) to separate the unwanted precipitate from the solution, 20mM of CuSO4•5H2O (calculated from total volume of lysate, estimated around 50 mL) was slowly added to the lysate solution – this was the "salting-out" purification step before running the sample through the FPLC. Upon addition of CuSO4•5H2O the solution immediately turned to a deep, opaque blue color, and the mixture was allowed to equilibrate for another 30 minutes before the solution was spun down. After separating out the unwanted precipitate, the remaining blue protein solution was then stored at 4°C for at least 24 hours before purification via FPLC. The blue protein solution had a typical volume of 50 mL, and at this stage, despite the goal of producing only Cu^{II}Az48W, the solution contained a mixture of Cu^{II}Az48W and Zn^{II}Az48W because of the unavoidable presence of Zn^{II} during the growth and lysis steps.

1.2.3 Az48W FPLC Purification and Cyanide Dialysis

Prior to injecting the sample into the FPLC column, the blue sample from above was exchanged into ~ 150 mL of 1 mM sodium acetate buffer at pH 4.5. The buffer exchange was performed using a 50 mL Amicon ultrafiltration cell with a 10 kDa ultrafiltration disk (Millipore). The purification of Az48W was completed in the same method as previously described[15] using a cation-exchange column (Source 15S column, GE Healthcare). The solutions used for equilibrating the column were 1 mM and 250 mM sodium acetate buffers at pH 4.5. The 1 mM sodium acetate buffer solutions used for the buffer-exchange (Amicon) step and the FPLC process were

from the same stock. After purification through the FPLC column, the samples were de-metallated through cyanide dialysis. The previously established protocol for cyanide dialysis[15,16] was implemented. However, some changes were made. For successful de-metalation of holo-Az48W, a protein sample stock of 1 mM in a total volume of 3 mL was injected into a 3 mL dialysis cassette (3500 MWCO Slide-A-Lyzer cassette). The sample was dialyzed in a 1 L solution of 0.5 M potassium cyanide dissolved in 100 mM pH 8.0 phosphate buffer. Three rounds of dialysis with KCN were completed, in which each round was 2 hours long. After each 2-hour cycle, the old buffered KCN solution was replaced with fresh cyanide-phosphate buffer. The dialysis beaker was surrounded with ice during the entire 6 hours of cyanide dialysis. After the third exchange into fresh KCN buffer, the sample was placed in pH 8.0 phosphate buffer and dialyzed overnight at 4°C to remove the excess cyanide. The sample was washed once more with pH 8.0 phosphate buffer for 4 hours before exchanging via dialysis into the preferred buffer for apo-Az48W storage. Az48W apoprotein stocks with high concentrations (greater than 1 mM) were stored in pH 4.5, 50 mM sodium acetate (NaOAc) buffer. The apoprotein form of Az48W was used to make ZnIIAz48W and ND- ZnIIAz48W (refer to section 3.2.2). Since apo-Az48W has a high affinity for CuII, it was important that all containers used to store the apoprotein were washed with concentrated EDTA (250 – 500 mM EDTA solution).

1.2.4 Metalation with Zn^{II}

The metalation of azurin proceeded from the previous cyanide dialysis step, without removing the apoprotein from the dialysis cassette (however, concentration

adjustment may need to be made, see below). After exchanging the solvent to 50mM NaOAc buffer, the dialysis cassette with apoprotein was placed in a 1 L solution of 7 mM $ZnSO_4 \bullet 7H_2O$ dissolved in 50mM NaOAc buffer (pH 4.5). The buffer used for Zn^{II} dialysis should have an acidic pH (pH 4.5), since ZnSO4 has low solubility at neutral or alkaline pH (i.e. precipitates out in pH 7.2 – 8.0 phosphate buffer). A second round of dialysis with 7mM $ZnSO_4$ was completed to ensure that the protein stock was fully incorporated with the Zn^{II} metal. It was observed that high protein concentration stocks were harder to metallate with ZnSO4; therefore, a protein concentration of maximally 500 μM in a sample volume of 3 mL is recommended. Inductively coupled plasma mass spectrometry measurements (ICP-MS from the ECAL lab) were performed in order to check that the concentration ratio of Zn^{II} to protein was at least 1:1 and ensure that there was minimal CuIIAz48W contamination. In all samples discussed here, the amount of Cu^{II} contamination was<1%. The reason for pure sample is because radical yield results would vary if there were Cu^{II}- or apo- Az48W present in the stock samples. For example, it was noted that apoAz48W does not generate stable, neutral radical, which would cause an artificially lowered radical quantum yield. After metalation, the high concentration protein stock samples were stored in pH 4.5 sodium acetate buffer.

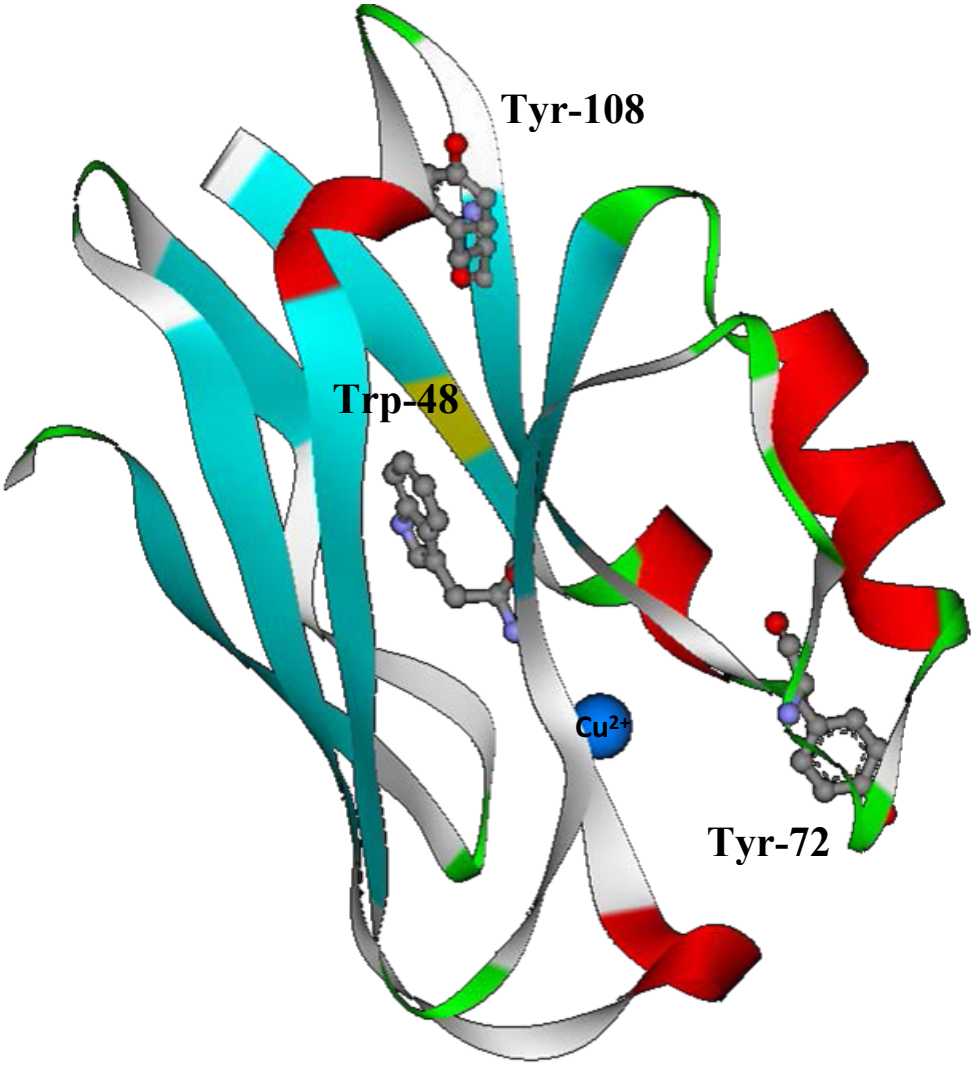

Figure 1.1: Crystal structure of native wildtype azurin with Cu^{2+}metal center. The Trp-48 and neighboring tyrosine residues are displayed. PDB ID: 5AZU.

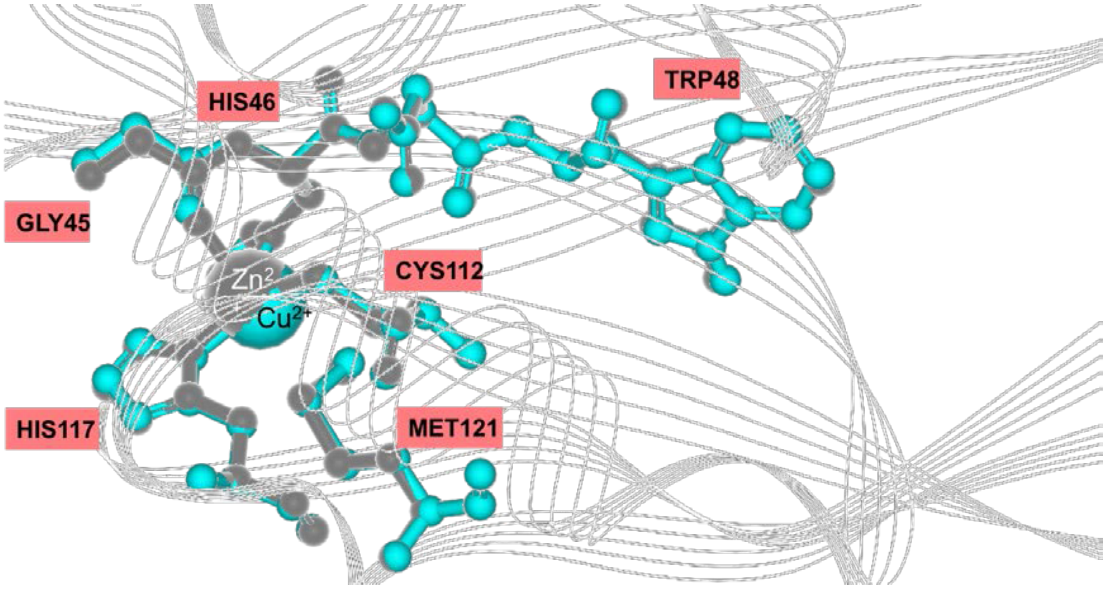

Figure 1.2: Metal coordination sphere of Cu(II) and Zn(II) derivatives of wildtype Azurin. AzWT-Zn^{II} (PDB: 1E67) is tethered and overlaid with the native azurin structure, AzWT-Cu^{II} (PDB: 5AZU). There are small differences for the Zn^{II} metallated wildtype azurin: the Met-121 residue is moved away from the Zn_{II} center, and the ZnII metal is closer to the Gly-45 residue[17].

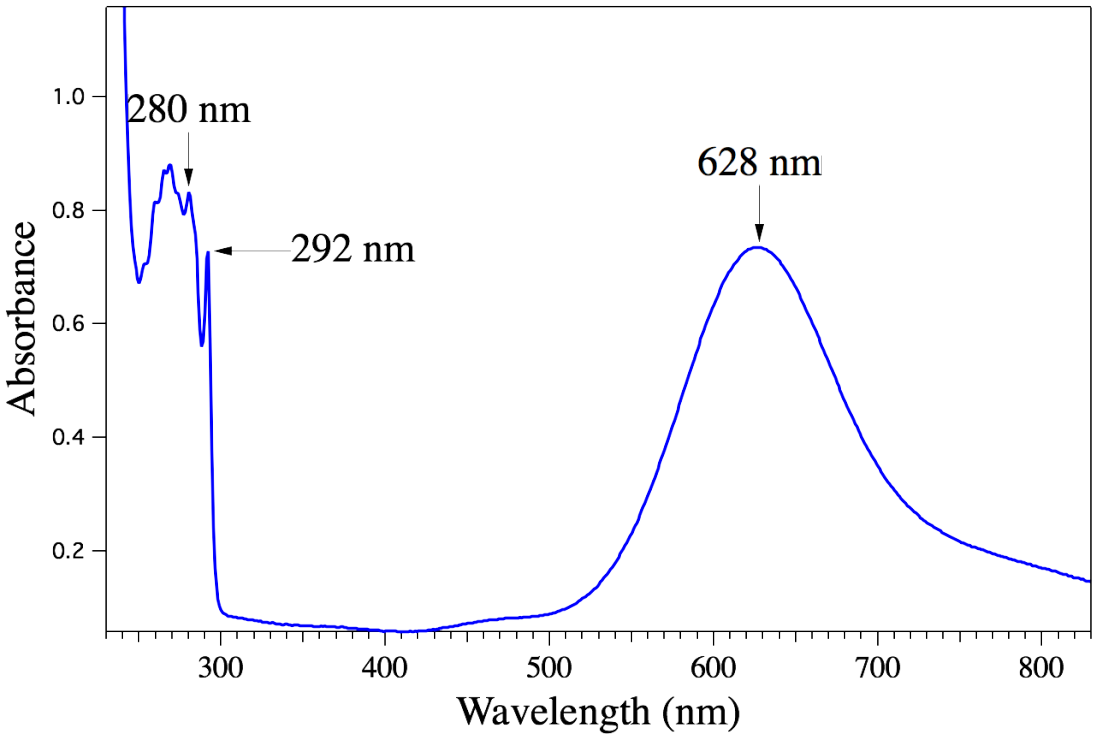

Figure 1.3: Absorption spectrum of Cu^{II}-Az48W mutant, with the LMCT band indicated at 628 nm. The broad absorption at 628 nm represents the LMCT band seen in type I copper proteins, where the molar absorptivity is measured to be 5900 $M^{-1}cm^{-1}$. Aromatic amino acids absorb 280 nm light, and the single tryptophan residue absorbs 292 nm light. The ratio of absorbance at 280 nm (ε280 = 6690 M^{-1} cm^{-1}) to 292 nm (ε280 = 5817 $M^{-1}cm^{-1}$) is characteristic of the azurin protein, and can be used to quantify the purity of mutant samples.

2 Vibrational Modes

2.1 Introduction

Resonance Raman spectroscopy is a form of vibrational spectroscopy based on inelastic scattering that provides environmental and structural information of a given molecule[18,19]. This method offers advantages over off-resonance Raman spectroscopy because the resonance condition in which the incident excitation wavelength overlaps with an electronic transition, or absorption band, leads to amplification of the signal up to 10^6–fold. Resonance Raman shifts are characterized as Stokes or anti-Stokes inelastic scattering: in Stokes scattering, the energy of the scattered photon is lower than that of the incident photon, whereas in anti-Stokes scattering, the energy of the scattered photon is greater than that of the excitation photon. While both types of scattering take place, the probability of observing anti- Stokes scattered photons is low because in order for an anti-Stokes event to occur, there must be population in a higher- lying vibrational mode, which is only relevant for low-frequency modes or with high temperature. Therefore, in all spectra shown here, the peaks reflect Stokes scattering.

An important advantage of resonance Raman spectroscopy is the ability to reveal structural and environmental aspects of a single chromophore within large molecules – in this case, the chromophore is a naturally found trp-48 residue in a 14kDa azurin protein. By tuning the excitation wavelength to within the absorption band of tryptophan, there is minimal signal from the peptide backbone or other residues. Another key benefit of resonance Raman spectroscopy is that it can be performed on aqueous solutions without overwhelming interference from solvent

vibrations. These advantages allow resonance Raman spectroscopy to be a more effective vibrational technique than IR spectroscopy. In the present project, the excitation wavelength is tuned to enhance signal from the closed-shell tryptophan residue (UV resonance Raman) or the tryptophan radical (visible resonance Raman). With the use of both UV and visible wavelengths, structural and environmental information can be gained for the closed- and open-shell tryptophan-48 residue.

2.2 Materials and Methods

2.2.1 UV Resonance Raman with 228 nm excitation wavelength

The UV Resonance Raman setup for has been previously described[20]. Briefly, a tunable Ti:Sapphire laser is adjusted to 1kHz fundamental output of 912 nm; the resulting power ranges from 0.750 – 0.780 μW. The fundamental wavelength was collimated into a lithium triborate (LBO) crystal in order to generate the second harmonic wavelength of 456 nm (the polarization direction of the second harmonic is flipped 90 degrees after exiting the LBO crystal). The fourth harmonic wavelength was generated using a β-barium borate (BBO) crystal, resulting in the desired 228 nm wavelength used to excite the Az48W protein samples (the polarization of the fourth harmonic flips again, regenerating the same polarization as that of the infrared fundamental). The fourth harmonic light was dispersed using a Pellin-Broca prism, where the 228 nm wavelength was isolated. The power of the UV light after the Pellin-Broca prism and the UV turning mirror ranged from 4 to 7 mW. The UV-Resonance Raman spectra presented here were collected with UV power of ~4 mW.

The Az48W protein samples were flowed through a vertical quartz capillary,

with an outer diameter of 160μm and inner diameter of 102μm. The angle between the incident light and the capillary is 135°, in a backscattering conformation. For 228 nm, the spectrograph was centered at 707 nm, and a 3600 grooves/mm holographic grating dispersed the light; this configuration had the net result of the center wavelength of 235.6 nm on the detector. The pre-filter slit was set to 110 μm, and the intermediate filter slit was set to 2.13 mm. The sample was flowed using a syringe pump at a rate of 0.16 mL/min. Acetonitrile was used to calculate the signal counts to ensure efficient collection of scattered light for a given experiment; the peak at 918.9 cm^{-1} was monitored, and the counts per second were normalized with the power measured. The acetonitrile spectrum was used to calibrate the pixels to Raman shift (cm^{-1}); the day-to-day pixel calibration can result in Raman shift errors of ±1 cm^{-1}. For all samples, the gain of the CCD detector was set to 2, with a 100kHz readout rate.

Each sampled protein had a concentration of 25 μM in a total volume of 2 mL. The integration time was 60 seconds, with 12-13 cycles that totals to 12-13 minutes of total resonance Raman spectra collection. The protein samples were all diluted in pH 7.2 phosphate buffer (made with protiated, ultrapure water), and background spectra of the phosphate buffer was collected in the same manner as the protein samples.

2.2.2 Visible Resonance Raman with 514 nm and 488 nm Excitation Wavelengths

The laser setup of the visible resonance Raman (visible RR) and general data analysis of the collected spectra have been previously described[10]. A mixed-gas Kr- Ar laser (Coherent Innova 70C) was used, and the laser output was tuned to 514 nm or 488 nm, with the laser aperture set at 7. An interference filter (either 514 nm or 488 nm, depending on the chosen incident wavelength) was placed in front of the exit slit of the laser. In order to prevent Rayleigh scattered light from entering the spectrograph, an appropriate edge filter was placed directly in front of the entrance slit of the spectrograph (Jobin Yovin iHR 320). The spectrograph contained a 1200 grooves/mm grating and a CCD detector. The bandpass was 10 cm^{-1} and corresponded to a spectrograph entrance of 100 μm. The readout rate was set to 20 kHz during visible RR data collection. With 514 nm excitation, the spectrograph was centered at 557 nm and 549 nm for D5-Zn^{II}Az48W• and H5-Zn^{II}Az48W• samples, respectively. With 488 nm excitation, the spectrograph was centered at 527 nm for analysis of both D5-Zn^{II}Az48W• and Zn^{II}Az48W• samples. For both 488 nm and 514 nm excitations, the signal counts (at Gain 2) were determined using spectroscopy grade ethanol, in which the normalized counts per second per mW were based off the 883.3 cm^{-1} peak of ethanol. Acetonitrile (spectroscopy grade) was used to calibrate the pixels, in order to convert to Raman shift (cm^{-1}) values. Again, the day-to-day acetonitrile pixel calibration can have an error of ±1 cm^{-1}.

For all visible RR analyses, the scattered light was collected at a 90° angle with respect to the incident light. The protein samples were diluted to 25 - 50μM with pH 7.2 phosphate buffer. The $[Co^{III}(NH_3)_5Cl]Cl_2$ (referred to as Co^{III}) concentrations were

approximately two times greater than the protein concentration. Power-dependence studies, not discussed in this thesis, have indicated that there is no photodamage up to 14 mW; the incident power for the spectra reported here was 4-6 mW. There were no new peaks seen (indicative of photodegradation byproducts) during the span of the collection time. The power was measured at the sample position (above the final focusing lens).

The samples remained in an atmosphere-controlled quartz cuvette, with the dimensions of 2 mm x 10 mm. Each sample was deoxygenated (exchanged with Ar gas) prior to visible RR collection. The photolysis setup for generation of the neutral radical species is discussed in Section 3.2.4. Pre-photolysis visible RR spectra were collected for 2-3 hours, then the samples were irradiated for 30-40 minutes, and subsequent post-photolysis visible RR spectra were collected for the same amount of time (2-3 hours). For each collection period, the integration time was 60 seconds with a total of 30 cycles. This collection period was repeated 4-6 times for a total of 2-3 hours.

2.2.3 Density Functional Theory Calculations and Vibrational Mode Assignments

Density functional theory calculations were performed with B3LYP functional using Gaussian 09W, and mode assignments were based off established mode descriptions for tryptophan, as discussed previously[10,21]. There are a few differences in the current 3EI calculations compared to literature[10]: the basis set was changed to 6-311+G(d,p) and the input structure of closed and open shell 3EI (3-ethylindole) were non- coplanar (Figure 2.1). This non-coplanar condition was derived from the crystal structure (Figure 1.1). The mode displacements were viewed using both GaussView[22]

and a web-based graphic program, ChemCraft[23]. ChemCraft retains the same vibrational frequencies and corresponding mode displacements as displayed in GaussView. In order to quantify the similarities between normal modes of different isotopologues, a web-based application, Vibalizer[24], was used. The input structure of both closed and open shell 3EI had a non-coplanar angle of 113.9°. With the equilibrated output molecule of 3EI, the perdeuterated 3EI isotopologue vibrational modes (for closed and open shell 3EI) can be obtained by directly changing the indole C-H bonds to C-D bonds in GaussView (re-optimization is not necessary after isotopic exchange). The isotopic shifts calculated between perdeuterated and protiated 3-EI closed shell normal modes were used to guide the assignments of the experimental vibrational frequencies of D5-Zn^{II}Az48W. The vibrational modes of Zn^{II}Az48W have been discussed[25], and can be identified with comparison to experimental UV resonance Raman of H5-L-trp and the D5-L-trp analog (spectra taken from Dr. Hannah Shafaat). However, with the closed and open shell Zn^{II}Az48W, there are a few labeling differences observed compared to previously published identifications[10,25]. The differences in labels are attributed to the different 3-EI input structure used for the calculations (non-coplanar vs. coplanar conformation in previous work). The new mode labels for Zn^{II}Az48W and Zn^{II}Az48W• are based off both non-coplanar, 3EI calculations and the comparison to established modes[26] of experimental L-trp in solution.

The vibrational modes of closed and open shell ND-Zn^{II}Az48W are based off of NATA (open and closed shell) calculations and literature mode assignments for indole ND- L-trp and ND- NATA[21,26]. The input structures of NATA and NATA• are

non-coplanar (Figures 2.2 and 2.3) and mimicked the angle of Trp-48 in wildtype Cu^{II}-Azurin (5AZU structure, Figure 1.1). After optimization, the NATA isotopologues were generated directly from GaussView. The closed shell NATA isotopologue had all exchangeable protons deuterated, while open shell form had only the amide backbone deuterated. The vibrational modes were compared and identified using the previously mentioned web-based applications.

2.3 Results

2.3.1 Vibrational Modes of Closed Shell D5-Zn^{II}Az48W

Vibrational modes of both the closed shell protiated and perdeuterated Zn^{II}Az48W are shown in the 228-nm UV resonance Raman spectrum in Figure 2.4. Spectra of the model compounds D5-L-trp and H5-L-trp are also shown. The nomenclature for the fully protiated form of Zn^{II}Az48W will be abbreviated as H5-Az48W (representative of H5NH-Az48W) while the perdeutero derivative will be labeled as D5-Zn^{II}Az48W (representative of D5NH-Zn^{II}Az48W). The isotope shifts for both closed shell and open shell perdeuterated Az48W are determined with density functional theory calculations of 3-ethylindole (3EI), using a B3LYP functional and 6-311+G** (6-311+G(d,p)) basis set. The original input structure of 3EI has a non-coplanar dihedral angle of 113.9° in order to roughly mimic the 114.9° angle of trp-48 observed in native Az48W (refer to crystal structure in Figure 1.1). The output structure of 3EI is shown in Figure 2.1. After equilibration of the structure in the calculation, the dihedral angle of the closed shell 3EI shifts to 113.88°. In comparing fully protiated Zn^{II}Az48W (H5-Zn^{II}Az48W) to its perdeutero isotopologue, there is an

overall downshift in the majority of normal modes of closed shell D5-Zn^{II}Az48W. The W18, W17, and W16 modes for perdeuterated D5-Zn^{II}Az48W are significantly downshifted when comparing the UV Raman spectrum of the protiated form. The W18, W17, and W16 vibrational modes of D5-Zn^{II}Az48W have isotopic downshifts of 52 cm^{-1}, 54 cm^{-1}, and 164 cm^{-1}, respectively. Additionally, the W12 and W10 modes have significant downshifts of 102 cm^{-1} and 48 cm^{-1}, respectively. The perdeuterated W7 mode at 1340 cm^{-1} loses the distinctive second peak, as seen in the protiated W7 normal mode, and develops a shoulder at a 1330 cm^{-1}.

With 228-nm excitation, the intensity ratio of W18 to W16 modes changes in the spectrum of D5-Zn^{II}Az48W. In H5-Zn^{II}Az48W, the ratio for W18:W16 is 1.40, while that of D5-Zn^{II}Az48W is 0.50, indicating the greater W16 intensity seen in the perdeuterated spectrum. As seen in Figure 2.4, the overall intensity differences can be distinguished in the normalized vibrational spectra of both protiated and perdeuterated Zn^{II}Az48W protein. In addition to the aforementioned W18:W16 intensity ratio, the W13 and W1 vibrational modes also exhibit different relative intensities for the isotopologue. Both the W13 and W1 normal modes of D5-Zn^{II}Az48W have increased intensities compared to the protiated spectrum.

Table 2.1 presents an overall summary of Zn^{II}Az48W and L-tryptophan normal mode assignments, along with the respective deuterated and protiated derivatives. The calculated isotope shifts are compared to experimental data to help identify the normal modes in D5-Zn^{II}Az48W. Additionally, comparison with spectra of model compound, L-trp, and published results supports the assignments.

2.3.2 Vibrational Modes of D5-Zn^{II}Az48W Neutral Radical

Visible Resonance Raman spectra of tryptophan neutral radical (W48•) is observed with both 514nm and 488nm excitations (Figure 2.5). The 514 nm excitation shows larger Raman cross-sections because 514 nm overlaps with the absorption maximum (refer to Figure 2.6). Table 2.2 provides a comparison of the isotopic shift observed in experimental results and theoretical 3-EI• calculations, where the input dihedral angle for the structure of 3-EI• is the same as the closed shell calculation for 3-EI previously mentioned. Figure 2.1 shows the calculated output structure of 3-EI• with the angle optimized to 112.85°. Table 2.3 compares the calculated vibrational frequencies of H5-3EI• and D5-3EI• to the corresponding experimental peaks of H5-Zn^{II}Az48W• and D5-Zn^{II}Az48W• spectra. The scaling factor of Table 2.3 represents the scaling factor needed to match the calculated and experimental results in the visible Resonance Raman spectra of Figure 2.5. The general trend is that the scaling factor is a value less than 1.00, indicating that the majority of calculated values are higher than the experimental frequencies; however, there are a few exceptions where the scaling factor is greater than 1.00, representative of calculated vibrational modes with lower frequency than the experimental labels. In either direction, the scaling factors deviate from unity by only 3%. Overall, the calculations serve as a guide for the expected isotopic shifts between perdeuterated and protiated neutral radicals of Zn^{II}Az48W to aid in mode assignments.

As expected, the isotopically substituted Az48W neutral radical (D5-Zn^{II}Az48W•) have downshifted vibrational frequencies relative to the protiated radical (H5-Zn^{II}Az48W•) spectra, as summarized in Table 2.1. With 514 nm excitation, the

greatest isotopic shifts are seen in W17•, W16•, W12•, and W4•, all of which result in a significant downshift with the exception of the W12• mode. The W17•, W16•, and W4• modes are downshifted by 59 cm^{-1}, 178 cm^{-1}, and 66 cm^{-1}, respectively, relative to the protiated radical; the W12• normal mode of perdeuterated neutral radical is at a higher frequency, with a 56 cm^{-1} upshift, compared to that of the protiated radical. Table 2.2 summarizes the difference in isotopic shifts observed between calculated and experimental values. The Δ_{iso} ratios display the overall differences between expected isotopic shifts of 3-EI• and the observed shifts of Zn^{II}Az48W• seen in the visible resonance Raman spectra of Figure 2.5.

The neutral radical of the perdeuterated isotopologue has different relative peak intensities for the W19•, W14•, W7•, W4•, and W2• normal modes. The W19• mode, apparent only with 514 nm excitation, has an expectedly lower frequency (located at 521 cm^{-1}) in the deuterated analog and becomes broader with a shoulder near 542 cm^{-1}. The W14•, W4•, and W2• peaks have greater intensities in D5-Zn^{II}Az48W• than in H5-Zn^{II}Az48W•. The W7• mode loses its distinct peak in the perdeuterated isotopologue compared to the doublet observed in the protiated radical.

Some changes are noted with 488 nm excitation compared to 514 nm. The low-frequency W19• mode disappears with 488 nm excitation, as shown in Figure 2.5. In both perdeuterated and protiated derivatives of Az48W•, the W1•, W2•, W3•, and W7• modes retain most of its peak intensities when comparing the two excitation wavelength spectra. Furthermore, the shapes of the aforementioned peaks remain consistent going from 514 nm to 488 nm excitation.

2.3.3 Vibrational Modes of Closed Shell ND-Zn^{II}Az48W

UV Resonance Raman with 228 nm excitation wavelength was used to distinguish the differences between protonated and deuterated indole rings, i.e. ND-Zn^{II}Az48W vs. NH-Zn^{II}Az48W. The nomenclature for the fully protiated form will be abbreviated as NH-Zn^{II}Az48W (representative of H5NH-Zn^{II}Az48W) while the singly-deuterated form will be labeled as ND-Zn^{II}Az48W (representative of H5ND-Zn^{II}Az48W). The most notable changes are the downshifts of W17, W12, W10, and W6 modes upon deuteration of the exchangeable indole proton, as seen in Figure 2.7. The W17 mode of ND-Az48W has a 22cm^{-1} downshift and a slightly lowered intensity compared to the protonated counterpart. Table 2.4 lists the isotopic shifts for Zn^{II}Az48W where the experimental shifts are compared to calculated model compounds NH-NATA (N-Acetyl-L-Tryptophanamide) and ND-NATA vibrational frequencies. Figure 2.2 shows the corresponding calculated output structures of NH-NATA and ND-NATA, where ND-NATA is deuterated at all exchangeable protons on the indole ring and backbone ("B" of Figure 2.2). The W10 mode displays an upshift of 9 cm^{-1} and 6 cm^{-1} for experimental and calculated modes, respectively. The relative intensities of all modes are nearly identical between protonated and deuterated analogs, with the exception of an increased intensity for the W6 normal mode for in ND-Zn^{II}Az48W.

2.3.4 Vibrational Modes of Neutral Radical of ND-Zn^{II}Az48W

As expected, the visible resonance Raman spectrum (514 nm excitation) of the neutral radical in Figure 2.8 (A) shows nearly identical normal modes for the neutral

radical of ND-Zn^{II}Az48W and NH-Zn^{II}Az48W; this strong similarity is expected because the radical is deprotonated, and the only difference between the two species is the deuterated backbone that was not exchanged during dialysis back into H_2O (refer to Materials and Methods section 3.2.2). The considerable differences are denoted as the peaks marked in Figure 2.8 (A) – these are additional peaks observed for ND-Zn^{II}AzW48•. Another difference is observed for the W10• mode, with a higher frequency (upshift of 8 cm^{-1}) compared to the NH-Zn^{II}Az48W• spectrum. These differences are qualitatively reproduced in the calculations of NATA•, where the protonated and deuterated forms of NATA• include either H or D on the amide backbone of the model compound, respectively (the deuterated form is seen in "B" of Figure 2.3). The W10• mode has a calculated upshift of 5 cm^{-1} for the backbone deuterated NATA•, while additional peaks denoted with asterisks are also calculated ("B" of Figure 2.8). While the calculation of the model compound does not take into account the possibility of multiple-deuterated backbone, it nonetheless predicts changes in the spectrum of the radical ND-Az48W• spectrum that is observed experimentally.

2.4 Discussion

The two deuterated isotopologues of azurin studied here (D5-Zn^{II}Az48W and ND-Zn^{II}Az48W) exhibit varying isotopic shifts and intensities compared to the protiated forms. The UV Resonance Raman spectrum of closed shell azurin derivatives were taken using 228 nm excitation, an incident wavelength that overlaps with the strong, deep-UV absorption band present in most proteins and aromatic

molecules. ND-Zn^{II}Az48W is analogous to the protonated form of Zn^{II}Az48W, except that the exchangeable proton on the indole ring is deuterated, substituting N-H to N-D. Since this isotopologue is a singly-deuterated species, the vibrational frequencies of closed shell ND-Zn^{II}Az48W is similar to NH-Zn^{II}Az48W, with exceptions for modes that include displacement of the indole N-H group. On the other hand, the perdeuterated form of Zn^{II}Az48W (D5-Zn^{II}Az48W) is expected to exhibit significant differences in the vibrational spectrum because all the hydrogen atoms in the trp-48 indole ring are deuterated, while the N-H moiety remains unsubstituted. Through the exchange of C-H to C-D bonds, the normal modes of closed shell tryptophan will result in noticeably different vibrational frequencies due to the substitution of five heavier atoms on the indole ring. The shift of these modes seen in the closed shell forms provide vibrational information that can underlie the functionality and mechanism of ET in perdeuterated and singly-deuterated Az48W.

Comparison of D5-Zn^{II}Az48W and H5-Zn^{II}Az48W. Differences in relative intensities and frequencies are observed for the perdeuterated isotopologue (see Figure 2.4). In H5-Zn^{II}Az48W, the W18 and W16 modes have a well-characterized intensity ratio, where the W18 mode has a greater intensity than the W16 mode with 228nm excitation. In contrast, the W18:W16 intensity ratio for D5-Zn^{II}Az48W has the opposite trend, where the W18 mode is less intense than the W16 mode. In resonance Raman spectroscopy, absolute intensities of specific vibrational modes of a chromophore reflect the extent of the geometry difference between the ground and resonantly- excited electronic states. The intensities of normal modes are also wavelength-dependent, and a plot of Raman scattering cross-section for each normal

mode as a function of excitation wavelength (called a Raman excitation profile) is needed to fully understand the origin of intensity differences between D5-Zn^{II}Az48W and H5-Zn^{II}Az48W. In this study, an excitation profile was not pursued so further insights into the differences in intensities are not offered.

Aside from changes in relative intensity, it appears that there are different peaks in the D5-Zn^{II}Az48W spectrum compared to H5-Zn^{II}Az48W. For example, the 740 cm^{-1} peak (marked on Figure 2.4) in D5- Zn^{II}Az48W is not present in the model compound D5-L-tryptophan, and the analogous peak in H5- Zn^{II}Az48W is also not observed. We are continuing to investigate the origin of this unidentified peak. The W7 doublet in H5-Zn^{II}Az48W is another example that is not observed in D5-Zn^{II}Az48W; this W7 mode peak difference can be clarified with the corresponding comparisons between H5-L-trp and D5-L-trp. The W7 doublet arises from coupling between different vibrational modes in H5- L-trp, and these couplings are not present in D5-L-trp because the vibrational frequencies for D5-L-trp are different from protiated L-trp.

A significant effect in deuterating Zn^{II}Az48W is the large isotopic shifts associated with exchanging the trp-48 indole moiety with heavier deuterium atoms. In closed shell D5-Zn^{II}Az48W, most normal modes have lower vibrational frequencies compared to the protiated form, H5-Zn^{II}Az48W (Figure 2.4). The vibrational signatures that exhibit the largest downshifts are the W18, W17, W16, W12, and W10 normal modes. These exceptionally large downshifts, up to 164cm^{-1} (as seen in the W16 mode of D5-Zn^{II}Az48), reflect the change in C-H vibrational frequency upon deuteration to C-D. With the heavier deuterium substitutions,

Raman vibrational frequencies are expectedly lowered. Brief analysis of the W18, W16 and W12 modes supports this expected trend: the W18 mode is the in-plane ring- breathing vibration of the indole ring, the W16 mode is focused on the benzene in- plane breathing vibration, and the W12 mode represents the in-plane C-H bending mode localized primarily on the benzene ring. Upon H/D exchange, these vibrations exhibit large downshifts because the frequency of a harmonic oscillator with larger mass decreases. Both the W17 and W10 modes have indole N-H motions in addition to motion of ring bonds, and these modes are sensitive to changes in hydrogen- bonding properties[19]. Even though the indole N-H moiety is not deuterated in D5- Zn^{II}Az48W, the W17 mode has a significant downshift caused by the isotopic substitution along the C-H bonds of the indole ring.

Comparison of ND-Zn^{II}Az48W and NH-Zn^{II}Az48W. The closed shell ND-Zn^{II}Az48W vibrational modes have a few notable downshifts in the W17, W12, and W6 vibrational frequencies (Figure 2.7). The singly-deuterated N-H moiety on the indole ring has been previously identified[21,26] to have a large downshift of approximately 20 cm^{-1} for the W17 mode, which is expected since the W17 mode is characteristic of N-H displacement. Similarly, the W6 mode also has a large downshift of at least 40 cm^{-1} due to the N-D isotopic substitution. The W6 mode is a combination of indole stretching, benzene C-H bending, and N-H bending[21]. The W12 mode also includes N-H displacement along the indole ring, and exhibits an isotopic downshift of 15 cm^{-1}. Although upshifts are uncommon upon isotopic substitutions, there is an occurrence of such anomalies, as seen in the W10 mode. A simplistic explanation of this higher vibrational frequency upon deuteration is that the overall normal mode is

perturbed in such a manner that the resulting vibrational frequency is higher for N-D than for N-H. The DFT calculations of closed shell ND- NATA (Table 2.4), which includes H/D exchange of the backbone ("B" of Figure 2.2), is consistent with the isotopic shifts noted in the experimental spectrum.

Comparison of neutral radicals of isotopologues. Visible resonance Raman spectroscopy was used to analyze the vibrational structures of the neutral radicals of the Zn^{II}Az48W isotopologues (Figure 2.5 and Figure 2.8). Since the peak absorption band of the radical is at 515 nm (Figure 2.3.6), resonance Raman excitation with 514 nm excitation wavelength enhances signal from only the neutral radicals.

Significant changes in vibrational frequencies and intensities are observed for D5- Zn^{II}Az48W• compared to H5-Zn^{II}Az48W•. The intense W19• band is present in both the perdeuterated and protiated Zn^{II}Az48W neutral radicals. In a previous publication[10], the W19• mode was identified as an in-plane breathing displacement of the indole ring. The significant downshifts of the W17•, W16•, and W4• modes for D5-Zn^{II}Az48W• are due to the previously mentioned heavy-atom effect on the C-H (or C-D) bending modes. The small upshift of the W12• mode is caused by a similar effect as described for the higher frequency shift observed in the W10 mode of closed shell ND-Zn^{II}Az48W. The increased intensities of the W14•,W4•, and W2• modes may reflect differences in excited-state and ground-state structures of the perdeuterated radical compared to the protiated radical; however, a full analysis of the Raman excitation profile is needed to confirm the nature of the intensity differences. In addition to enhancement of known peaks, there is also an appearance of new peaks seen in D5-Zn^{II}Az48W•. In the spectrum of D5-Zn^{II}Az48W•, new peaks appear

relative to the protiated analog, observed in in the lower vibration frequency region (850– 950 cm^{-1}) of Figure 2.5.

The spectrum of the radical resulting from ND-Zn^{II}Az48W should, in principle, be identical to the radical from the protonated NH-Zn^{II}Az48W species because the radical is deprotonated. However, there are a few differences that reflect unavoidable deuteration of some regions of the amide backbone (displayed in Figure 2.8). In the process of generating the ND-Zn^{II}Az48W species, the protein is completely unfolded and refolded in D_2O-based buffer (refer to Section 3.2.2). Despite subsequent dialysis into H_2O-based buffer, some protected amide regions remain deuterated once Zn^{II}Az48W is refolded. Calculations of NATA• with a deuterated amide backbone reproduce the few peak shifts observed between the ND-Zn^{II}Az48W• and NH-Zn^{II}Az48W• spectra (Figure 2.8).

Overall, the visible Resonance Raman can characterize the novel isotopologue species of Zn^{II}Az48W• while the UV Resonance Raman of the closed shell derivatives can provide insight into the electron and proton transfer process of azurin.

Table 2.1. Closed Shell Zn^{II}Az48W and D5-Zn^{II}Az48W normal modes, with comparisons to calculated 3- ethylindole (3EI) and experimental L-tryptophan isotopic shifts. All Raman shifts are in cm^{-1}, and all isotopic shifts, indicated as Δ_{iso}, are also in cm^{-1}.

Trp Mode	Calculated 3EI Isotopic Shift, $\Delta_{iso,\ 3EI}$	% Similarity[a]	Expt. H5-L-Trp	Expt. D5-L-Trp	$\Delta_{iso,\ LTrp}$[b]	Expt. H5-Zn^{II}Az 48W	Expt. D5-Zn^{II}Az 48W	$\Delta_{iso,\ Az48W}$	Δ_{iso} Ratio[c]
W18	-54	30.7%	760.9	708.4	-52.6	759.3	707.06	-52.2	0.994
W17	-76	54.1%	882.7	826.3	-56.4	874.1	820.03	-54.0	0.958
W16	-170	36.7%	1014.1	854.6	-159.6	1011.7	848.16	-163.5	1.025
W13	-280	45%	1120.8	1029.1	-91.7	1075.8	1003.10	-72.7	0.793
W12	-343	48.7%	1158.9	1052.6	-106.3	1158.8	1056.60	-102.2	0.9614
W10	-43	72.9%	1243.4	1211.0	-32.4	1235.1	1199.10	-36.0	1.11
W7	-8	68.5%	1360.6	1339.7	-20.9	1359.3	1340.40	-18.9	0.904
W4	-55	73.1%	1517.8	1445.7	-72.1	1520.0	1440.90	-79.1	1.10
W3	-28	91.0%	1552.7	1526.0	-26.7	1555.3	1528.40	-26.9	1.01
W2	-25	94.4%	1579.3	1562.9	-16.4	1605.0	1586.40	-18.6	1.13
W1	-20	96.5%	1618.1	1601.8	-16.3	1623.6	1605.00	-18.6	1.14

[a]The similarity percentage is taken from a web-based application that quantitatively compares the mode displacements between two species.
[b]The isotopic shifts between H5-L-Trp and D5-L-Trp were based on spectra taken acquired by Dr. Hannah Shafaat.
[c]The ratio of the isotope shift for L-Trp and the corresponding normal mode shift for Az48W is calculated as a ratio of $\frac{\Delta iso,Az48W}{\Delta iso,LTrp}$.

Table 2.2. Normal mode assignments of Zn^{II}Az48W• and D5-Zn^{II}Az48W•, with comparison to isotope shifts in calculated protiated and perdeuterated 3-ethylindole (3EI) neutral radical.

TRP• MODE	Calculated [a]H5-3EI• (cm^{-1})	Calculated [b]D5-3EI• (cm^{-1})	PERCENT SIMILARITY[c]	Calculated ISOTOPIC [d]SHIFT (cm^{-1})	Expt [g]H5-AZ48W• (cm^{-1})	Expt. [h]D5-AZ48W•	Expt. ISOTOPIC [e]SHIFT (cm^{-1})	Isotopic Shift Ratio[f]
W19•	526	511	78.9%	-15	539	521.02	-18	1.2
W18•	761	713	53.4%	-48	754.8	711.99	-42.8	0.89
W17•	857	797	43.8%	-60	837.0	778.09	-59.0	0.98
W16•	1026	825	11.3%	-201	1003.1	810.94	-192.2	0.956
W14•	1048	1034	33.1%	-14	1069	1035.2	-34	2.4
W13•	1120	1078	26.7%	-42	1146.1	1098.6	-47.5	1.1
W12•	1156	1206	33.3%	50	1161.8	1218.2	56.4	1.1
W10•	1198	1147	29.4%	-51	1206.8	1145.9	-60.9	1.2
W7•	1369	1346	51.1%	-23	1342.4	1313	-29	1.3
W4•	1455	1379	32.3%	-76	1435.8	1370.4	-65.4	0.86
W3•	1484	1459	74.9%	-25	1456.6	1418	-39	1.5
W2•	1602	1574	89.8%	-28	1559.9	1530.9	-29.0	1.0
W1•	1628	1599	90.9%	-29	1591.6	1560.8	-30.8	1.1

[a,b]The calculated vibrational frequencies (in cm^{-1}) corresponding to each normal mode of protiated and perdeuterated 3-ethylindole neutral radical. [g,h]The experimental vibrational frequencies (in cm^{-1}) of H5-Zn^{II}Az48W• and D5-Zn^{II}Az48W•. [c]The labeled normal modes are reaffirmed with the percent similarities of mode displacements between H5-3EI and D5-3EI using a web-based application, Vibalizer.

[d,e,f]The calculated isotopic shift of 3-EI• is compared to the experimental shifts in Zn^{II}Az48W•, generating a ratio difference represented as $\frac{\Delta iso,exp}{\Delta iso,calc}$.

Table 2.3. Scaling factor relating calculated H5- and D5-3EI• to experimental H5- and D5- Zn^{II}Az48W• vibrational frequencies. All calculated and experimental frequencies are in cm^{-1}.

TRP• MODES	Calculated H5-3EI•	Experimental H5-AZ48W•	SCALING FACTOR	Calculated D5-3EI•	Experimental D5-AZ48W•	SCALING FACTOR
W19•	526	539	1.02	511	521.02	0.981
W18•	761	754.8	0.992	713	711.99	1.00
W17•	857	837.0	0.977	797	778.09	1.02
W16•	1026	1003.1	0.9777	825	810.94	1.02
W14•	1048	1069	1.020	1034	1035.2	0.9988
W13•	1120	1146.1	1.023	1078	1098.6	0.9812
W12•	1156	1161.8	1.005	1206	1218.2	0.9900
W10•	1198	1206.8	1.007	1147	1145.9	1.001
W7•	1369	1342.4	0.9806	1346	1313	1.025
W4•	1455	1435.8	0.9868	1379	1370.4	1.006
W3•	1484	1456.6	0.9815	1459	1418	1.029
W2•	1602	1559.9	0.9737	1574	1530.9	1.028
W1•	1628	1591.6	0.9776	1599	1560.8	1.024

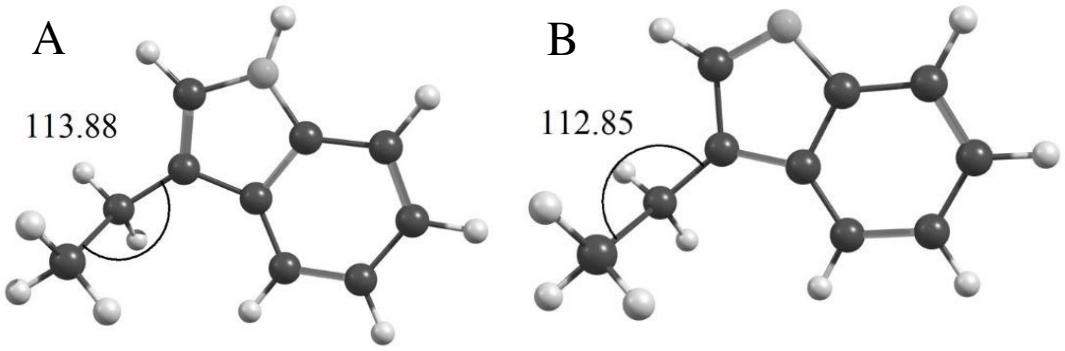

Figure 2.1: Optimized configurations of closed and open shell 3-ethylindole (3EI) calculations, derived from Gaussian. The protiated closed (A) and open shell (B) configurations are displayed with optimized dihedral angles marked (in degrees). The optimization was performed in Gaussian and the display of both the angle and molecule are from ChemCraft[22]. The perdeuterated forms (not shown) of the closed and open shell (D5-3EI and D5-3EI•, respectively) have the same configurations, except with the H/D isotopic exchange along the indole rings (C-H to C-D only).

Table 2.4. Comparison of isotopic shifts between experimental, closed shell Zn^{II}Az48W and calculated, closed shell N-acetyl-L-tryptophanamide (NATA) upon isotopic exchange of the N-H indole moiety. All calculated and experimental frequencies are in cm^{-1}.

Trp Mode	Calc. NH- NATA[a]	Calc. ND- NATA[b]	% Similarity[c]	Isotopic Shift[d]	Expt. NH-Zn^{II}W48[e]	Expt. ND-Zn^{II}W48[f]	Isotopic Shift[g]
W17	888	862	76.0%	-26	874	852	-22
W12	1184	1179	70.7%	-14	1158	1143	-15
W10	1238	1244	59.2%	6	1235	1244	9
W6	1462	1423	20.3%	-41	1493	1455	-38

[a,b,c]Calculated vibrational frequencies, along with percent similarities from *Vibalizer*, of NH-NATA and ND-NATA, where the amide acidic hydrogens are also deuterated in the calculations. [d]The isotopic shifts of calculated NATA, where ND-NATA has H/D exchange of all hydrogens found on the indole ring and amide bond. [e,f,g]The experimentally determined vibrational frequencies and isotopic shifts of Zn^{II}Az48W.

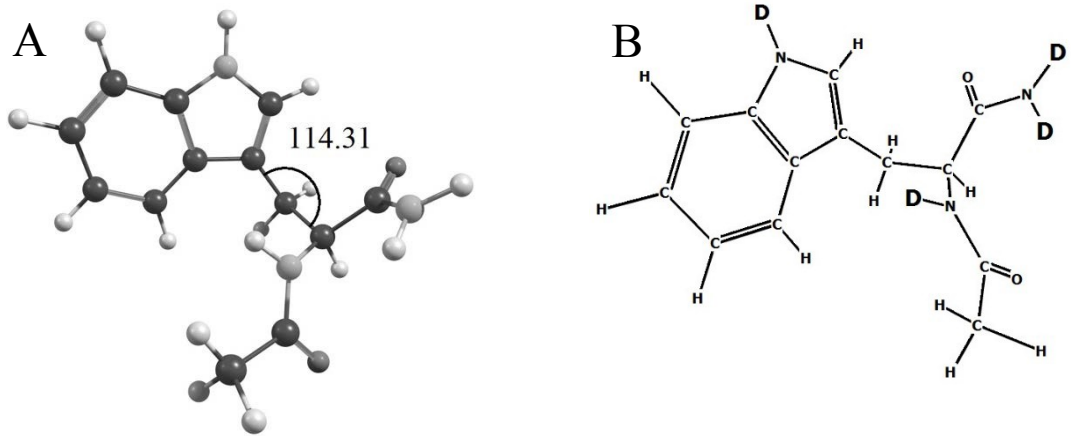

Figure 2.2: Closed shell protiated and deuterated configurations for N-acetyl-L-tryptophanamide (NATA) DFT calculations. The protiated, closed shell form of NATA is displayed with the optimized dihedral angle marked (A). The deuterated form of NATA has isotopic exchanges for all acidic hydrogens, including the N-H moiety of the indole ring and the amide and amine groups of the backbone (B). The optimized configuration (using Gaussian) of the deuterated NATA is identical to the protiated form. The display of both the molecule and the angle is taken from ChemCraft[22].

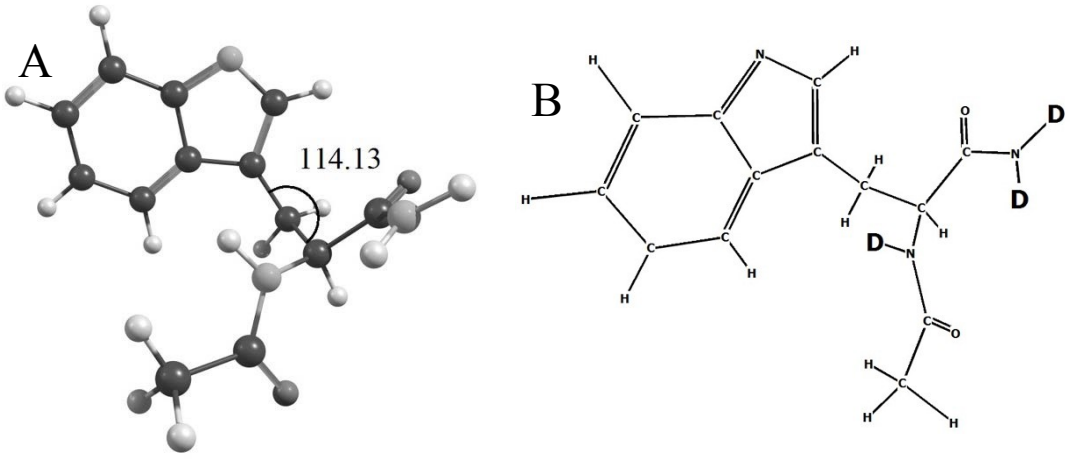

Figure 2.3: Open shell protiated and deuterated configurations for NATA• (N-acetyl-L-tryptophanamide neutral radical) DFT calculations. The protiated, open shell form of NATA• is displayed with the optimized dihedral angle marked (A). The deuterated form of NATA• has H/D exchanges for all acidic protons of the amide and amine groups (B). The optimized configuration (using Gaussian) of the deuterated NATA• is identical to the protiated form. The display of both the molecule and the angle is taken from ChemCraft[22].

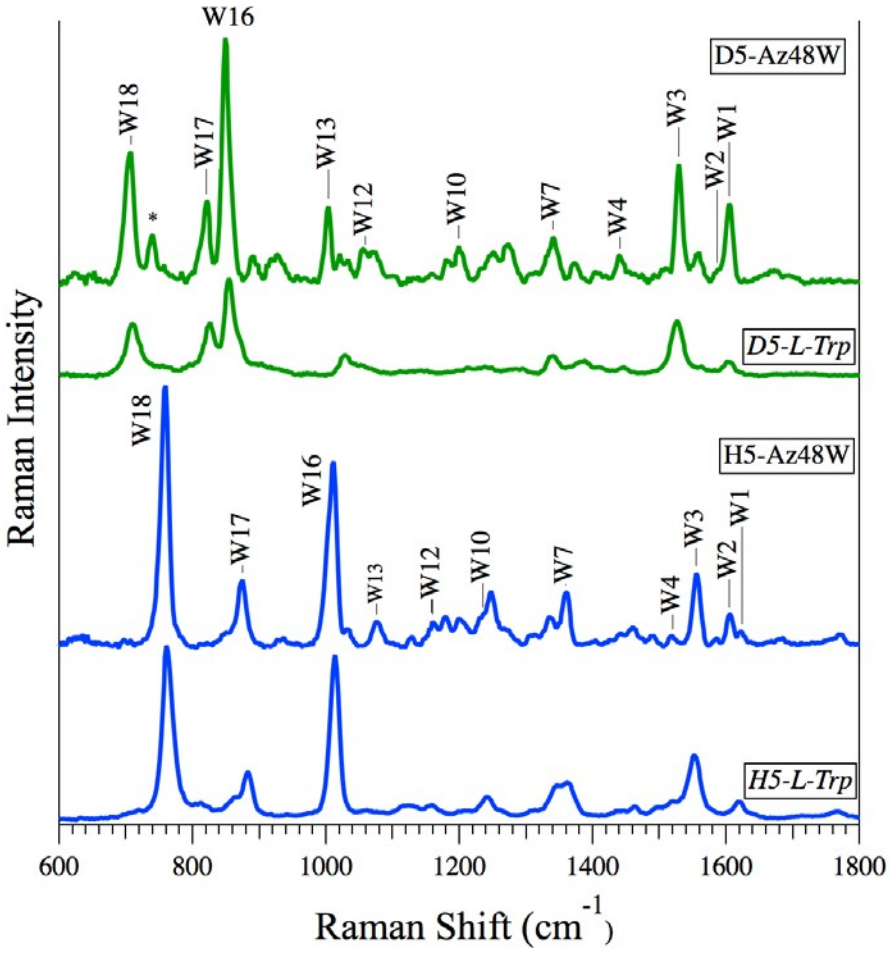

Figure 2.4: UV Resonance Raman spectra with 228 nm excitation of closed shell D5-Zn^{II}Az48W, H5-Zn^{II}Az48W, D5-L-Trp, and H5-L-Trp in pH 7.2 phosphate buffer. The normal vibrational modes are labeled for the closed shell perdeuterated (D5-Zn^{II}Az48W) and fully protiated (H5-Zn^{II}Az48W) protein spectra. The corresponding L-tryptophan spectra are designated by either H5-L-Trp (protiated) or D5-L-Trp (perdeuterated). The asterisk marks an enhancement of a peak at 740 cm^{-1} that is present only in D5-Az48W UV Resonance spectrum. Both perdeuterated and protiated L-trp spectra were acquired by Dr. Hannah Shafaat.

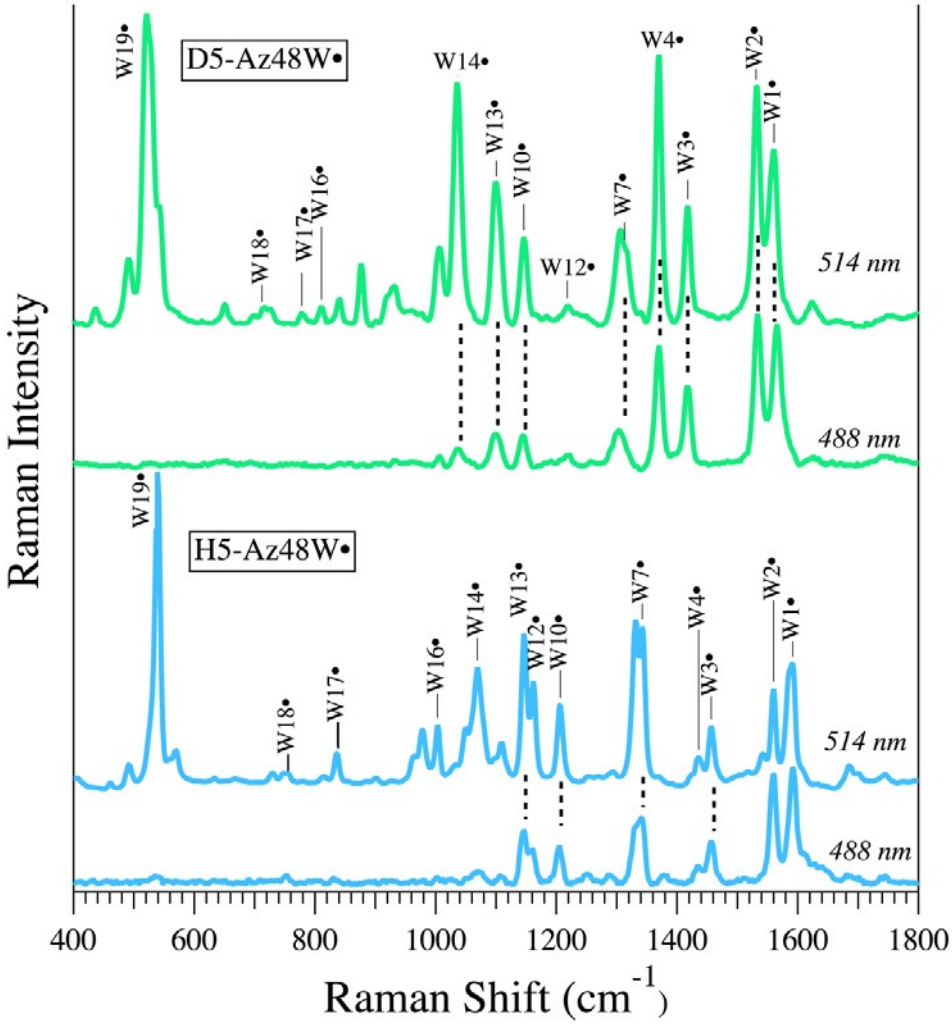

Figure 2.5: Visible Resonance Raman spectra with 514 nm and 488 nm excitation of neutral protein radicals, D5-Zn^{II}Az48W• and H5-Zn^{II}Az48W• in pH 7.2 phosphate buffer. Both visible resonance Raman of the perdeuterated (D5-Zn^{II}Az48W•, top) and fully protiated (H5-Zn^{II}Az48W•, bottom) neutral radicals are displayed, with excitation wavelengths of 514 nm (top overlays) and 488 nm (bottom overlays). The peaks that are seen present in both 514 nm and 488 nm excitation are linked with dashed lines.

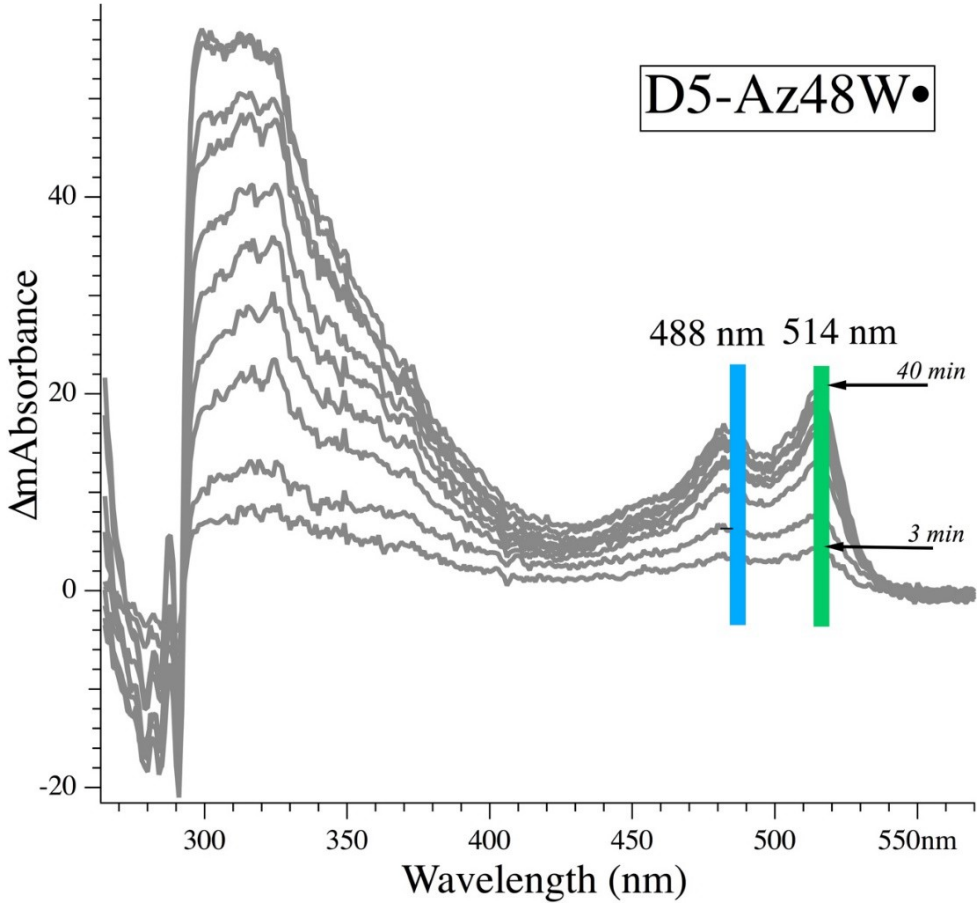

Figure 2.6: Difference absorption spectra of D5-Zn^{II}Az48W• with visible Resonance Raman excitation wavelengths indicated. The difference absorption spectra after photolysis of D5-Zn^{II}Az48W are shown, where the growth of D5-Zn^{II}Az48W• during 40 minutes of photolysis is observed as the rise in intensity at 482 nm and 514 nm. visible peak. The excitation wavelengths used to obtain the visible Resonance Raman spectrum of D5- Zn^{II}Az48W• are indicated, in which Raman analysis is taken after 40 min of photolysis. Both protiated and perdeuterated Zn^{II}Az48W• have identical absorbance profiles at the 482 and 514 nm regions.

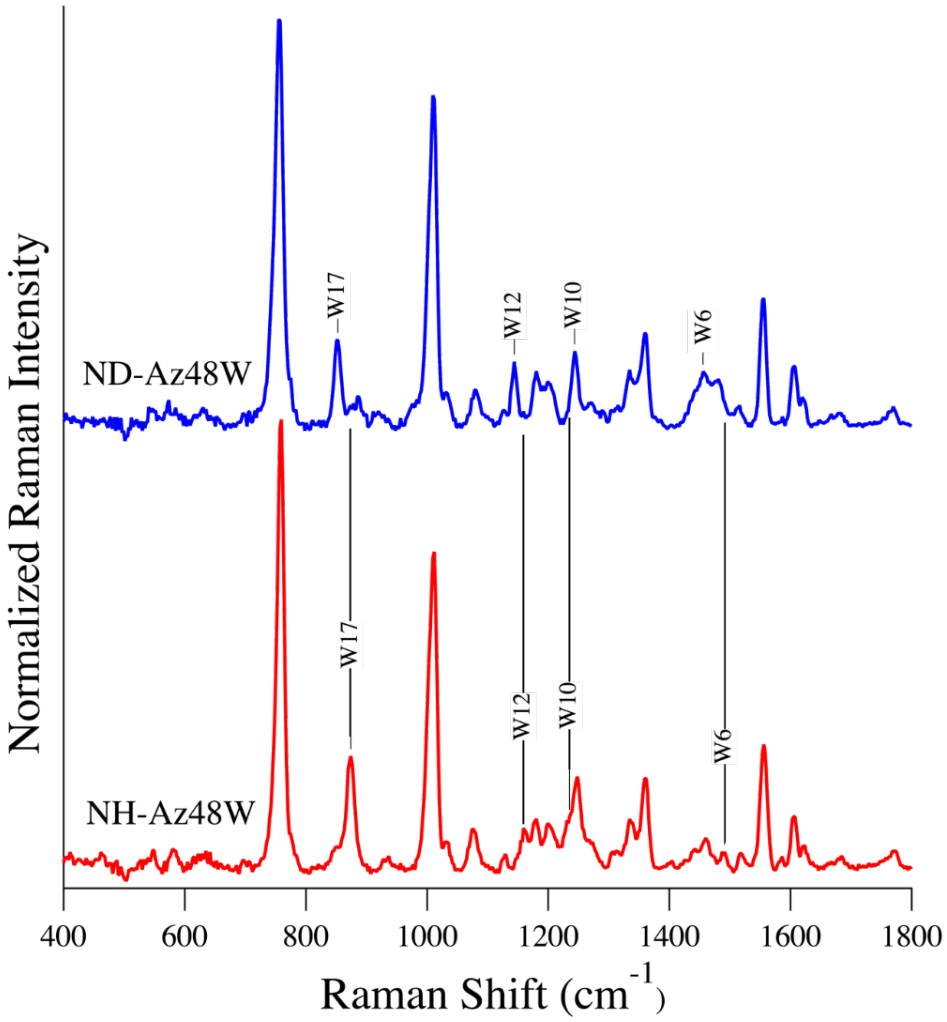

Figure 2.7: UV Resonance Raman spectra with 228 nm excitation of closed shell, fully protiated NH-Zn^{II}Az48W and closed shell, singly-deuterated ND-Zn^{II}Az48W, in pH 7.2 phosphate buffer. The UV resonance Raman of ND-Zn^{II}Az48W (top) and NH-Zn^{II}Az48W (bottom) are displayed. The normal modes that are shifted upon isotopic substitution are marked with respect to the NH-Zn^{II}Az48W modes of W17, W12, W10 and W6. The intensities are normalized by concentration of protein.

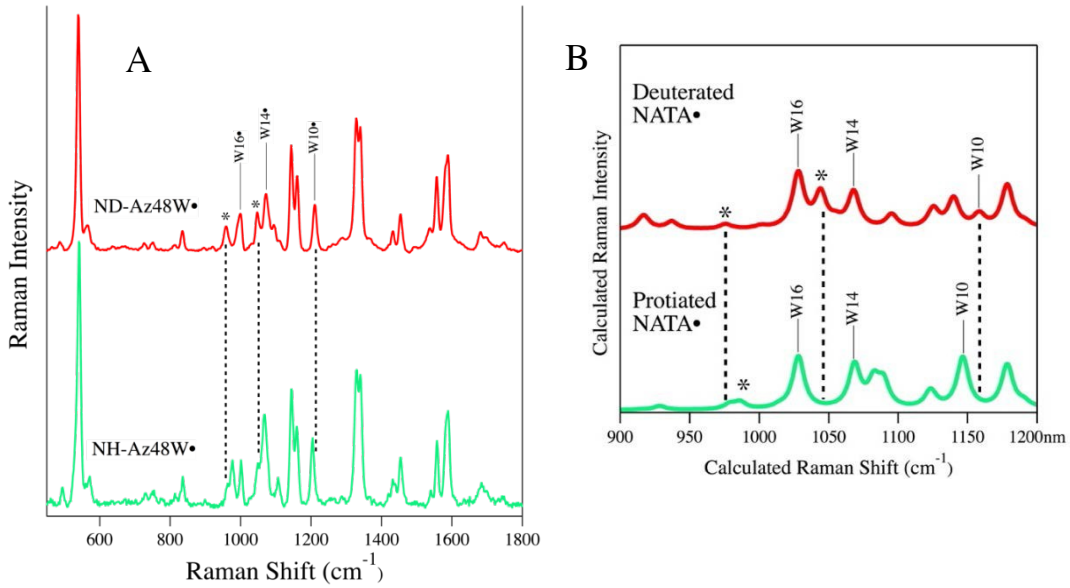

Figure 2.8: Visible Resonance Raman spectra with 514 nm excitation of ND-Zn^{II}Az48W• and ND-Zn^{II}Az48W• in pH 7.2 phosphate buffer, with comparison to calculated deuterated and protiated NATA• spectra. The comparison of visible resonance Raman spectra of ND-Zn^{II}Az48W• to NH-Az48W• is displayed (A), where the primary differences between the two spectra are indicated (*). The calculated spectra of backbone protiated and deuterated NATA• are shown in (B). The corresponding differences in the calculated spectrum of fully protonated NATA• compared to the deuterated form are marked (*). Deuterated NATA• has deuterons for all acidic hydrogens on the amine and amide groups (refer to Figure 2.3).

3 Fluorescence and Radical Quantum Yields

3.1 Introduction

Experiments to determine quantum yields for radical formation and fluorescence were performed to explore the electron and proton transfer reactions that lead to the formation of neutral radical. The fluorescence quantum yield is interpreted in the context of the photoexcitation and subsequent electron transfer process for tryptophan oxidation. The radical quantum yield reflects the overall efficiency of formation of the neutral radical, which is dependent on the final deprotonation step. Fluorescence is a common spectroscopy technique that can provide information on excited state lifetimes, quenching activity by external acceptors, and environmental aspects of a chromophore. Fluorescence is simply defined as the process of photon emission resulting in electronic relaxation from the excited state, S_1, to the ground state, S_0. A solvent-exposed chromophore will exhibit fluorescence quantum yields that reflect interactions with bulk solvent. In contrast, if the chromophore is embedded in a solvent-inaccessible, folded protein environment, the quantum yield reflects other interactions between protein and chromophore, and excludes bulk solvent. In-depth information on fluorescence can be found in several textbooks, notably the widely-used reference book by Lakowicz[27].

Az48W has a unique fluorescence profile and peak position because the trp-48 chromophore is embedded in the hydrophobic pocket of the protein. The fluorescence peak (λ_{max}) of fully folded Az48W is blue-shifted to 306nm with a narrow profile, while denatured azurin exhibits a broad band with low intensity, and a red-shifted λ_{max} of 357nm (Figure 3.1). Relative fluorescence quantum yield studies of each

isotopologue are described in this chapter, where values are compared to the known Φ_{fluor} of the model compound, N-acetyl-L-tryptophanamide (NATA). Along with external quenching, there are other competitive, non-radiative processes that can decrease fluorescence quantum yield: electron transfer, intersystem crossing, internal conversion, and energy loss in the form of heat to solvent. These competitive processes will be discussed in the context of the quantum yields for radical formation. The rate of formation of the neutral radical is also investigated here. This rate reflects the efficiency of proton transfer in Az48W and hence, is a critical aspect of the mechanism of radical formation. A previously published[8] study of Zn^{II}Az48W discussed the mechanisms, including pathways of ET/PT (electron transfer with stepwise deprotonation) and formation of neutral radical in the Zn^{II}Az48W mutant studied here.

The ability of azurin to stabilize a neutral tryptophan radical makes it an ideal system for studies of amino acid radicals. The tryptophan radical is most efficiently formed in the absence of tyrosine residues, and therefore, the native tyrosine residues are replaced with less polar phenylalanine residues. Previous work from our group showed that the presence of the native tyrosine residues (Tyr-72 and Tyr-108) can donate electrons to the tryptophan cation radical, $W48^{+}\bullet$, and rapidly reform the closed shell W48. Another essential criteria for formation of neutral radical in azurin is the replacement of the innate Cu(II) cofactor with redox inactive Zn(II) metal, which eliminates the possibility of intra-protein ET between Trp48 and Cu(II). A brief observation of the significance of a metal cofactor will be presented in this chapter, through photolysis of apo-Az48W. The first half of this chapter will be focused on the

electron transfer pathway to an external acceptor, a proposed mechanism that is summarized in Figure 3.2.

As mentioned above, the deprotonation step is a critical event for formation of the neutral radical, and one goal of this chapter is to investigate this step. The published mechanism[10] of deprotonation is displayed in Figure 3.3. Briefly, after electron transfer to an external acceptor, the highly energetic and charged W48 cation radical is deprotonated and the proton exits into the solvent with a proposed pathway based on the crystallography structure of azurin. It has been proposed that the proton transfer pathway involves the pi-pi interaction between Trp-48 and Phe-110 which can facilitate proton tunneling from the hydrophobic pocket to the bulk solvent. Therefore, alterations in cation-pi and hydrogen-bonding interactions of the Trp-48 N-H moiety may affect the deprotonation rate of Zn^{II}Az48W isotopologues, consequently altering the quantum yield of the respective neutral radical form. The second half of this chapter will focus mainly on the effect of isotopic substitution on the radical quantum yield of D5-Zn^{II}Az48W and ND-Zn^{II}Az48W isotopologues, compared to the published data of protiated Zn^{II}Az48W.

Overall, the radical and relative fluorescence quantum yields of the Zn^{II}Az48W isotope derivatives can extend on previously proposed mechanisms of ET and PT. However, the complexity that comes from multiple competitive pathways in fluorescence does complicate the correlation between molecular excitation and electron transfer. Nevertheless, the quantum yields study of the aforementioned isotopologues can unveil certain aspects of proton-coupled electron transfer that cannot be observed solely with analysis of the protiated form of Zn^{II}Az48W.

3.2 Materials and Methods

3.2.1 D5-Zn^{II}Az48W Preparation

The perdeuterated isotopologue, D5-Zn^{II}Az48W, was provided by a previous student of the Kim Group, Greg Shimamura. The present summary is derived from his laboratory notebook. The D5-Zn^{II}Az48W mutant was grown using a minimal media recipe listed in previously literature[28], and not the LB media used for growth and protein expression of standard protiated Az48W. The cells (Invitrogen BL21 Star, DE3, competent cells) were directly fed D5-L-Trp (Cambridge Isotopes), dissolved in the minimal media prior to inoculation. The growth and expression protocol of D5-Zn^{II}Az48W mimicked the steps described previously in Section 1.2.1, with the exception that the large 6-L flasks contained minimal media in place of LB media. The 500 mL overnight starter still had cells grown in LB media. The lysis and purification steps were done in the same way as described previously, with the use of the same chemicals and FPLC configuration. Demetallation, followed by incorporation of the Zn^{II} center, was done in the same manner as stated in Section 1.2.4. The fluorescence and absorption profiles of D5-Zn^{II}Az48W exhibited minor differences compared to Zn^{II}Az48W, as shown in Figure 3.1.

3.2.2 ND-Zn^{II}Az48W Preparation

Conversion of NH-Trp48 to ND-Trp48 required unfolding the protein because Trp-48 is in a solvent excluded cavity, and H/D exchange does not take place when folded azurin is stored in D_2O for days. We pursued H/D exchange of apo-Az48W to avoid misligation of the metal center during the refolding process. The folding

energetics of the apoprotein and holoprotein (Zn^{II} or Cu^{II}) forms of azurin have been previously discussed[29], along with pH dependence on the folded stability of holo-azurin[30]. With these parameters in mind, the apoprotein form of Az48W was used to form ND-Az48W, bypassing the complexities of refolding with a metal ligand present. After the purification step of Az48W with FPLC, the Cu^{II} and Zn^{II} metals were removed via dialysis in cyanide solution. This dialysis procedure was the same as previously described in Section 1.2.3. The resulting apo-Az48W was stored in 50 mM sodium acetate buffer at pH ~4.5 for later use for generation of ND-Zn^{II}Az48W or Zn^{II}Az48W. The preparation of ND-Zn^{II}Az48W was separated into two parts: unfolding apo-Az48W in guanidinium hydrochloride and refolding the protein in buffered D2O solution. Standard protiated Zn^{II}Az48W was also handled in the same manner, except in H_2O, to determine if there were any detrimental effects of the unfolding-refolding process to the overall integrity of the protein.

After the dialysis step, apo-Az48W was unfolded using guanidium-HCl in buffered D2O. A 6M Guanidinium-HCl (GuHCl) stock was made with 50 mM sodium acetate buffer in D2O (99.9% purity, Sigma-Aldrich). The final pD of this 50mM sodium acetate buffer ranged from 4.70 to 4.90 (pH= pD ±0.4). The final concentration of the 6M GuHCl buffered D2O stock was checked with a refractometer, using the 50 mM sodium acetate buffer in D2O as the reference. The unfolding solution consisted of 3M GuHCl (diluted from the stock using 50 mM acetate buffer in D_2O) and approximately 500 μM of apo-Az48W in a total sample size of 2.5 mL. The concentration of guanidinium chosen for denaturing apo- Az48W was based off the unfolding curves of apo- and Zn^{II}-azurin variants in literature[31]. The

final sample volume for denaturation was selected based on the size of the dialysis cassette (0.5-3mL capacity, 3500 MWCO, Slide-A-Lyzer). The denatured apo-Az48W sample was equilibrated for 1-2 hours in 4°C before a 200 μL aliquot of the sample was checked on the fluorometer (Jobin Yvon FL3-11). The denatured protein sample should not be diluted before checking the fluorescence, since dilution of the guanidinium concentration could instantly refolding the protein. After equilibration of 1-2 hours in 4°C, the fully denatured protein should have a fluorescence intensity peak (λ_{max}) at 357 nm (refer to C' trace on Figure 3.1).

After apoAz48W was confirmed to be denatured via fluorescence, the concentrated 3M guanidinium was diluted out of the sample via dialysis with a Slide-A-Lyzer cassette (3.5K, 0.5-3mL capacity). A neutral pH 7.2 phosphate buffer was made in D_2O, with a total volume of 200 mL, for dialysis. The neutral pH is preferable for refolding of apoAz48W, in order to avoid protonation of the His-46 and His-117 residues noted in acidic pH buffers[30] (i.e. pH 4.5 sodium acetate buffer). The dialysis was performed overnight (for at least 12 hours) in room temperature. A 250 mL beaker was used for dialysis in order to fully submerge the cassette. In order to ensure that apo-Az48W was refolded in D_2O-based buffer, the buffer fluorescence was checked prior to the start of dialysis. When compared to H2O-based buffers, the water Raman band of D2O should appear at a blue-shifted wavelength of 315 nm. Since the 3M guanidinium present in the sample was only diluted by a factor 1/80 after overnight dialysis, a DG-10 desalting column (Econo-Pac 10DG, Bio-Rad) was used to eliminate residual guanidinium. The aim was to ensure that the residual guanidinium concentration, after dialysis and salt-exchange, was negligible and did

not cause partial denaturation of apo-Az48W. The sample was eluted with either 50 mM sodium acetate buffer (pD 4.9) or 20 mM phosphate buffer (pD 7.6) – both pH values this stage and would stabilize apo-Az48W and do not hinder the refolding process. The fractions of sample were collected, and the absorption (UV-Vis Spectrophotometer, Hewlett-Packard 8453) and fluorescence spectra were measured. The absorption and fluorescence spectral profile of refolded ND-apoAz48W is identical to fully protiated Az48W (refer to Figure 3.1).

After confirmation that the apo-Az48W was fully folded in D2O buffer, $ZnSO_4$ was added to the sample to a final concentration of 7 mM. This $ZnSO_4$ was derived from a stock solution of 60 mM $ZnSO_4 \bullet 7H_2O$ dissolved in 2 mL of pure D_2O (or buffered D_2O), and an aliquot of the stock was pipetted into the apoprotein solution, still in D_2O buffer. The $ZnSO_4$ dissolves readily in the neutral D_2O solution because the mass of solid needed for this concentration was relatively small (approximately 35 mg). After adding $ZnSO_4$ to the sample, the protein remained in D_2O buffer and was stored at 4°C overnight to equilibrate with the metal ion.

As a final step, all proteins were exchanged back to H_2O via dialysis. It was important to add the metal cofactor prior to exchanging the D_2O buffer with fully protiated, H_2O-based buffer. This conclusion is based on several attempts at forming pure ND-Zn^{II}Az48W (and not a mixture of ND- and NH-Zn^{II}Az48W) in which the metallation step occurred after dialysis into H_2O. Radical quantum yield studies showed that exchange of the D_2O buffer for H_2O right after removal of residual guanidinium via the DG-10 column , while the protein is still in apo-form, resulted in low-stability neutral radicals (the 515 nm band would decrease after a few minutes of

irradiation). This instability may be caused by a modified protein structure. The crystal structure of wildtype apo-azurin indicates that there are two possible forms of apo-azurin that may be in equilibrium when in solution[32]: one structure shows that the metal coordination sphere looks identical to the holoprotein form, and a second form has a water molecule (or solvent molecule) incorporated at the metal-binding site in place of the Cu^{II} metal. The presence of two structures of apo-azurin and observed reduction in radical stability indicated that a metal is necessary for a complete refolding of ND-Az48W prior to exchanging the sample with protiated buffer.

After overnight equilibration of azurin in the presence of 7 mM $ZnSO_4$, a 3-mL dialysis cassette was used to exchange the deuterated buffer to a protiated sodium acetate pH 4.5 buffer. The purity of the resulting ND-Zn^{II}Az48W sample was checked with UV resonance Raman by confirming the ~22 cm-1 shift of the W7 mode shown in Figure 2.7; this mode helps quantify the extent of NH-Zn^{II}Az48W contamination. The sample was also checked with ICP-MS to confirm that the sample was fully metallated with Zn^{II}.

3.2.3 Measurement of Fluorescence Quantum Yield

All fluorescence quantum yield experiments were performed with deoxygenated samples of D5-Zn^{II}Az48W, ND-Zn^{II}Az48W, and H5Zn^{II}Az48W. The concentrations of the proteins ranged from 15μM to 20 μM. For experiments with Co^{III}, $[Co^{III}(NH_3)_5Cl]Cl_2$ was 2x greater than that of protein. All samples were in pH 7.2 phosphate buffer. Each sample was deoxygenated using a Schlenk line prior to measuring absorption and fluorescence spectra. The sample holder was an

atmospheric-controlled quartz cuvette (dimensions 2mm x 10mm) that was attached to a small glass bulb that allowed for facile degassing. The protein sample was initially placed in the glass bulb; this bulb was separated from the cuvette by two Kontes valves that prevented the contents of the bulb to leak into the cuvette portion. The sample was subjected to repeated cycles of pumped-purge every five minutes for a total of 20 minutes. During the time between each pump-purge cycle, the sample was equilibrated with constant flow of argon gas while being stirred with a micro- stir bar. After deoxygenating, the sample was transferred from the bulb to the quartz cuvette via gentle shaking and tapping. An absorption spectrum of the sample was measured with a dual-beam UV-Vis (Shimadzu UV-3600), followed by measurement of a fluorescence spectrum using a fluorometer (Jobin Yvon FL3-11). The fluorescence was recorded with 292 nm excitation wavelength, and the emission was collected from 300 to 500 nm. The fluorescence emission was collected at a 90° angle relative to the incident light; excitation was along the 10 mm pathlength, and emission was along the 2 mm pathlength. The scanning speed was set to 1 nm per second (integration time was 1 second per step). The excitation and emission bandpass were set to 2 nm. After the acquisition of a fluorescence spectrum, and absorption spectrum was collected for samples with $[Co^{III}(NH_3)_5Cl]^{2+}$; in deoxygenated conditions, small amounts of neutral radical can be observed at 515 nm in the presence of the external Co^{III} acceptor. Fluorescence spectra of the pH 7.2 phosphate buffer were measured at the beginning and end of the experiment. The water Raman band, with a peak intensity at 324 nm, was used as an internal intensity standard to calibrate the fluorimeter for day-to-day fluctuations in lamp intensity. The fluorescence quantum yields of each Zn^{II}Az48W

derivative were determined based on the normalized fluorescence intensity of a model compound, N-acetyl-L-tryptophanamide (NATA), whose absolute quantum yield is published[33]; the spectrum of the model compound was measured on an earlier date. The experimental NATA sample was diluted in KPi buffer and deoxygenated in the same manner as the protein samples.

3.2.4 Measurement of Quantum Yield for Radical Formation

Photolysis Procedure. The photolysis experiments for D5-Zn^{II}Az48W, ND-Zn^{II}Az48W, H5-Zn^{II}Az48W, and H5-apoAz48W were performed in a similar way as previously discussed[9,15]. Briefly, deoxygenated samples (using the Schlenk line discussed in Section 3.2.3) were irradiated with UV light from a CeraLux 175W Xenon arc lamp found in an Aminco SPF- 500 system. The wavelength and bandpass of the incident light was set to 292 nm and 8 nm, respectively. The wavelength and bandpass were measured (Ocean Optics) to be 291.91 nm and 9.62 nm, respectively. During photolysis, the samples were stirred with a flattened, rectangular magnetic micro-stir bar placed at the bottom of the cuvette, away from the illumination path of the UV light. This rectangular stir bar was unable to lie horizontally/flat in the cuvette because it is too long for the 2 mm dimension of the cuvette; therefore, it could only spin in the vertical position. The samples were irradiated along the short path dimension (2 mm) for only 30 seconds at a time – the cuvette was taken out of the path of the 292 nm light and the entire volume was stirred every 30 seconds. Stirring was achieved by moving the cuvette across a large magnetic stir plate a few times every 30 seconds, making sure the magnetic stir bar moved up and down the cuvette to

ensure mixing along the entire height of the sample. This process was important for thorough mixing so the entire volume of the sample would be irradiated during the photolysis time. Absorption spectra (Shimadzu UV-3600) were collected along the 10 mm pathlength after every 5 minutes of photolysis; the photolysis time did not include the time spent for stirring via the magnetic plate. All samples were irradiated for 30-40 minutes, and the data for the first 15 minutes (linear fit taken between 3-min and 15-min marks) were used to calculate the rate of radical formation at 515 nm and this linear growth, in turn, determined the quantum yield for radical formation.

Potassium Ferrioxalate Actinometry. The power measured from the Aminco system, as described previously, was corrected with potassium ferrioxalate actinometry. The experimental steps and sample preparation were taken from literature[9]. An 800 μL solution of approximately 0.006M potassium ferrioxalate in 0.050 M H2SO4 was irradiated with 292 nm from the Aminco system in the same way as previously described for the Az48W protein samples. The solution was stirred using a micro stir bar and a magnetic stir plate every 30 seconds. In order to ensure that the potassium ferrioxalate did not degrade by over 10% of the initial concentration, the total irradiation time was 3 minutes. A reference sample was prepared at the same time as the irradiated sample; the reference sample was left in the dark during the 3-minute photolysis of the irradiated sample. Immediately after photolysis, 320 μL of both the reference and the irradiated samples were added to two separate vials that contained 1.28 mL of 0.1% (by mass) 1,10-phenanthroline solution, which led to a final sample volume of 1.60 mL. The 0.1% phenanthroline buffered stock solution was approximate, with the final mass of phenanthroline slightly lower than 0.1% of the

buffered solution (sodium acetate buffer). After the ferrioxalate and phenanthroline solutions were combined and allowed to equilibrate for 30 minutes, absorption spectra of the reference and the irradiated samples were measured. The absorbance at 510 nm was used to measure the concentration of ferrous ions generated from photolysis. The derivation for the quantum yield associated with the potassium ferrioxalate actinometer have been previously discussed[34]. For the single trial for the thesis, the pre-photolysis spectrum was not measured before irradiation, and the fraction of 292 nm absorption was assumed from a separate 0.012 M potassium ferrioxalate solution with 0.050 M H_2SO_4 diluted from the same stock. The fraction of absorption was calculated with the assumption that the dilution from 0.012 M to 0.006 M was precise, and hence, the absorbance at 292 nm also differs by half. With those assumptions in mind, the fraction of 292 nm incident light absorbed by potassium ferrioxalate was determined by averaging the absorbance values from 287 nm to 297 nm (this range takes into account the 10 nm bandpass of the excitation light) and correcting it with the dilution factor of 2x. The calculated quantum yield of the ferrous ions from potassium ferrioxalate was experimentally higher than the reference value for 292 nm excitation[34]. The published quantum yield of ferrous ions is 1.24 for 297/302 nm excitation, while the value determined from the Aminco setup was 1.62. Therefore, the power for the radical quantum yield calculations was corrected by multiplying the measured irradiation power by a factor of 1.31.

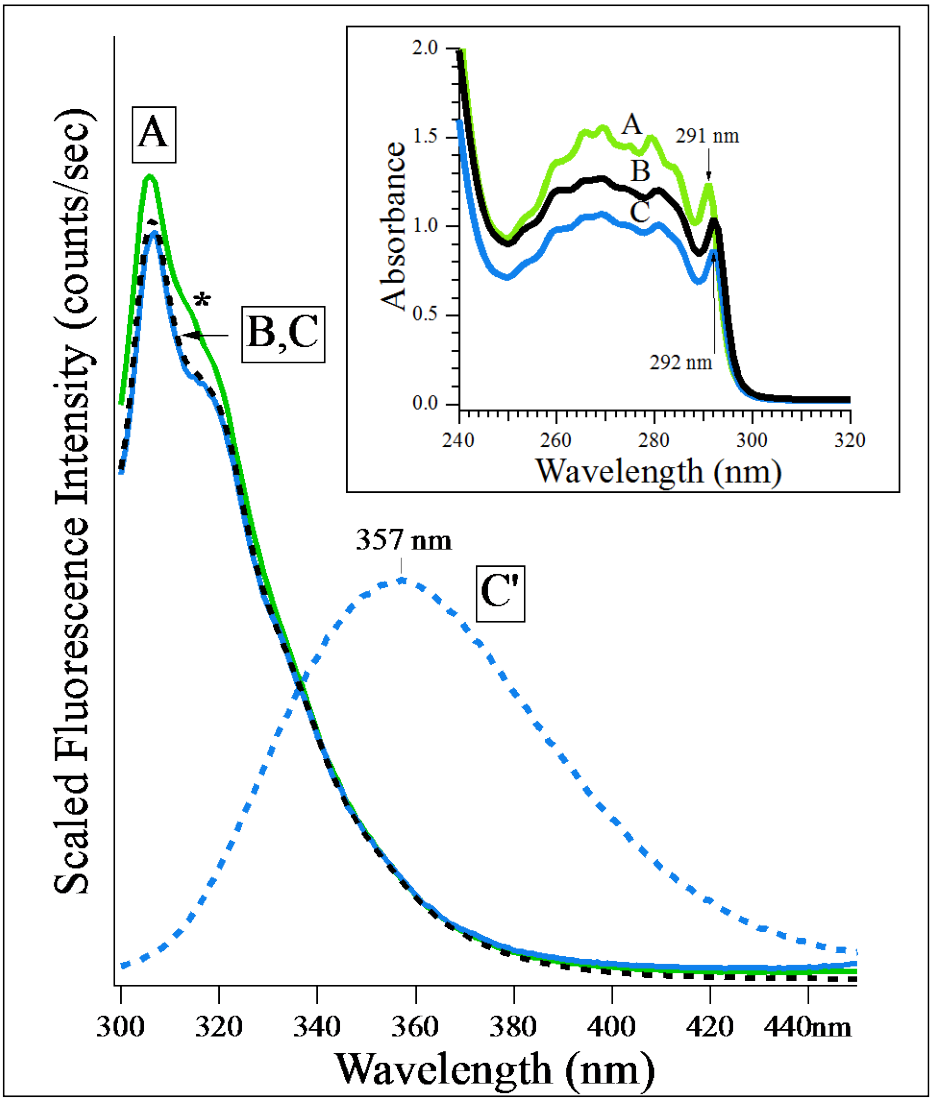

Figure 3.1: Fluorescence and absorption spectral profile of D5-Zn^{II}Az48W (A, green), Zn^{II}Az48W (B, black), and ND-Zn^{II}Az48W (C, blue) stocks. The fluorescence and absorption profiles for Zn^{II}Az48W and ND-Zn^{II}Az48W are nearly identical – the scaled fluorescence spectra overlaps well (B, C) and fluorescence λmax is at 307 nm for both species. The inset shows the UV absorption profile of the Azurin derivatives. The tryptophan absorption peak of ND-Zn^{II}Az48W (C) is seen at 292 nm, identical to the fully protiated form (B). The D5-Zn^{II}Az48W fluorescence profile (A) is skewed towards the higher energy wavelengths (slight blue shift), and the absorption spectrum indicates that the tryptophan absorbance peak is blue shifted by 1 nm unit compared to the H5-Zn^{II}Az48W and ND-Zn^{II}Az48W spectra. The spectrum of unfolded apo-Az48W, denatured in the presence of guanidinium hydrochloride, has a broad fluorescence, with a peak at 357 nm (C', blue dashed curve).

3.3 Results of Fluorescence and Radical Quantum Yield

Absolute fluorescence quantum yields of D5- Zn^{II}Az48W, ND- Zn^{II}Az48W, Zn^{II}Az48W, Cu^{II}Az48W, and apoAz48W. The fluorescence quantum yields of deuterated and protiated azurin are summarized in Table 3.1. The fluorescence quantum yield is determined by integrating the fluorescence emission from 300 to 400 nm, as indicated in the blue shaded region in Figure 3.4. The integrated fluorescence intensity is normalized by protein concentration and water Raman intensity, with the final units being counts per second per Molarity (cps/M). The final fluorescence quantum yield value is calculated in reference to the known value of the model compound, N-acetyl-L-tryptophanamide (NATA), in water. The overall Φ_{fluor} calculation is briefly summarized in the following equation (1).

$$(1)\ \Phi_{fluor} = 0.13 \times \frac{\text{Normalized Integrated Fluorescence } (\frac{cps}{M})}{\text{NATA Fluorescence in KPi } (\frac{cps}{M})}$$

The equation for fluorescence quantum includes the published value[33] for NATA in water, which has a fluorescence quantum yield of 0.13. Table 3.1 shows that the fluorescence quantum yields of D5-Zn^{II}Az48W, ND-Zn^{II}Az48W, and H5-Zn^{II}Az48W are 0.084, 0.167, and 0.19, respectively. The perdeuterated isotopologue has the lowest fluorescence quantum yield. In addition, the phosphorescence intensity relative to fluorescence is also listed, where D5-Zn^{II}Az48W has the lowest relative phosphorescence emission with a ratio of 0.0307. The phosphorescence ratio is taken as the ratio of phosphorescence and fluorescence peak intensities, seen in Figure 3.4, where the phosphorescence emission is in the range of 400 to 500 nm. Both H5-Zn^{II}Az48W and ND-Zn^{II}Az48W have similar phosphorescence ratios, with values of

0.032 and 0.034 respectively. In addition, the apoprotein form of protiated Az48W has similar fluorescence quantum yield of 0.18 and phosphorescence ratio of 0.0362, compared the holoprotein form (H5-Zn^{II}Az48W). The Cu^{II}Az48W mutant has the lowest fluorescence quantum yield at 0.0292; no phosphorescence is observed for this mutant. The absolute integrated fluorescence intensities are displayed in Figure 3.5, with error bars that reflect either the number of trials or the estimated error in calculations because of uncertainty in concentration.

Radical quantum yields of D5-Zn^{II}Az48W, ND-Zn^{II}Az48W, and apoprotein. The radical quantum yields of all Zn^{II}Az48W derivatives are listed in Table 3.2. For Zn^{II}Az48W species that generated neutral radicals, the radical quantum yields were calculated in the same way as previously published[8]. The simplified form, or definition, of the radical quantum yield is defined in equation (2).

$$(2)\ \Phi_{rad} = \frac{\text{Rate of W48 Radical Formed per Second, } k(\text{W48}\bullet)}{\text{Rate of W48 Excitation per Second, } k(\text{W48}*)}$$

Zn^{II}Az48W has the highest radical quantum yield of 0.127, ND-Zn^{II}Az48W has the second highest radical quantum yield of 0.086, while D5-Zn^{II}Az48W has the lowest neutral radical yield of 0.073. Figure 3.6 shows the photolysis of apo -Az48W, which failed to generate stable neutral radical even in the presence of Co^{III} external acceptor. The difference spectra of apoprotein Az48W, shown in the inset of Figure 3.6, has little enhancement at the 515 nm region, where the only positive absorption peaks near 350 nm are attributed to damaged protein and/or Co(II). Figure 3.7 shows an example difference spectrum during photolysis of ND-Zn^{II}Az48W, where the inset displays a linear fit that quantifies the rate of neutral radical formation (represented as ΔOD515

per minute). Using the slope and the incident power, the radical quantum yield was determined for each Zn^{II}Az48W derivative. Figure 3.8 displays the difference spectra for photolysis of ND-Zn^{II}Az48W, D5-Zn^{II}Az48W, and H5-Zn^{II}Az48W in a span of 30 minutes. The difference spectra are normalized with initial protein concentration and incident power, thus, clearly depicting the relative neutral radical yield for each species ($\Phi_{rad, D5} < \Phi_{rad, ND} < \Phi_{rad, H5}$).

3.4 Discussion

A comparison of the radical and fluorescence quantum yields can provide insights into the mechanisms of tryptophan-mediated PCET in azurin. The first half of this discussion will be based on molecular excitation and electron transfer, while the second half will focus on the deprotonation pathway that results in the formation of neutral radical. Collectively, these data may provide insights into the unique tryptophan radical in azurin and open up new experimental questions for further study.

Fluorescence quantum yield and electron transfer. The relative fluorescence quantum yield of each Az48W derivative is calculated in reference to the known Φ_{fluor} of N-acetyl-L-tryptophanamide (NATA) in water. The buried nature of Trp-48 results in a fluorescence intensity, with λ_{max} at 307nm, greater than that of NATA, a model compound that is completely exposed to the bulk solvent. As a result, the fluorescence quantum yields are higher for Zn^{II}Az48W and ND-Zn^{II}Az48W, where the Trp chromophore is protected from solvent accessibility and quenching. All samples are deoxygenated, which allows observation of the phosphorescence intensities for protein samples that lack an external acceptor (i.e. Co^{III}). Table 3.1 lists the relative

fluorescence quantum yields and the corresponding ratio of peak intensities of phosphorescence to fluorescence ($Intensity_{440\ nm}$: $Intensity_{307\ nm}$).

The fluorescence quantum yields of perdeuterated D5-Zn^{II}Az48W and singly-deuterated ND-Zn^{II}Az48W are compared to the protiated forms. ND-Zn^{II}Az48W and Zn^{II}Az48W have similar fluorescence quantum yields, whereas D5-Zn^{II}Az48W (which has an NH indole group) exhibits the lowest fluorescence intensity amongst all three Zn^{II}Az48W analogs. The decrease in fluorescence quantum yield for perdeuterated Az48W reflects non-radiative processes that compete with photon emission, such as intersystem crossing and internal conversion. Since the perdeuterated isotopologue has large differences in normal mode vibrational frequencies compared to the protiated species, as discussed in the previous chapter, the vibrational differences may potentially manifest in a change in the excited state lifetime (τ). Based on the semi-classical theory[35] (Marcus Theory) of electron transfer, the rate of ET is dominated by the reorganization energy (λ) and the electronic coupling term, H_{AD}. Therefore, with the decrease in all vibrational normal modes of D5-Zn^{II}Az48W, the overall lowered energetics can alter the electronic coupling between reactant and product (or donor and acceptor), decreasing the rate of electron transfer seen in the perdeuterated residue.

A simplified view of fluorescence quantum yield can be stated as follows: the quantum yield is the fraction of photons emitted per photons absorbed. Thus, by viewing the fluorescence quantum yield as directly proportional to the probability of deactivation of S_1 via photon emission, the fluorescence yield can be inferred as proportional to the excited state lifetime of the tryptophan reside in holoAz48W. This

correlation allows for interpretation of the fluorescence quantum yield in the context of ET probability from the S_1 state of Trp-48. If we assume that non-radiative processes are unperturbed by isotopic substitution, the differential fluorescence quantum yields may reflect quenching of S_1 by enhanced ET. This model is illustrated in the results for Cu^{II}Az48W, where the low fluorescence quantum yield is attributed to rapid charge transfer from photoexcited trp48 to the Cu(II) center[36.37]. This model can be extended to our system, where a low fluorescence quantum yield is expected to correlate to a high radical formation quantum yield if the ET process proceeds from the S_1 state. However, D5-Zn^{II}Az48W exhibits both a low fluorescence quantum yield and low radical quantum yield compared to ND-Zn^{II}Az48W and NH-Zn^{II}Az48W. This observation suggests that additional considerations must be taken into account. One possibility is that the low fluorescence intensity of perdeuterated Zn^{II}Az48W can be explained by a high internal conversion rate to ground state and hence, decreased excited state lifetime; if the ET reaction were to occur from S_1, this decreased lifetime would result in low radical yield. The fact that the vibrations of D5-Zn^{II}Az48W are different from protiated Zn^{II}Az48W could lead to enhanced non-radiative decay mechanisms that depopulate S_1 faster in D5-Zn^{II}Az48W* than in H5-Zn^{II}Az48W*.

Another possible explanation involves another significant non-radiative process that is known to take place in azurin, namely intersystem crossing (ISC) to the triplet T_1 state. Intersystem crossing is evident in the observed phosphorescence between 400 – 500 nm wavelengths for deoxygenated Zn^{II}Az48W samples in the absence of an external Co(III) acceptor. Comparing all three phosphorescence ratio intensities, the phosphorescence emission of D5-Zn^{II}Az48W is the least intense, while

ND-Zn^{II}Az48W has similar phosphorescence yield as Zn^{II}Az48W. The low phosphorescence observed in the perdeuterated isotopologue can, to a degree, provide another explanation of the low radical yield.

In current studies done by the Kim Group's Ignacio Lopez-Peña, the excitation of the triplet state (T_1) can induce a higher radical yield, compared to direct excitation of the singlet ground state, S_0. This observation provides evidence that the triplet state may play a role in the formation of the cation radical, $Az48W^{+}\bullet$. While definitive conclusions cannot be made at this time, it is hypothesized that the initial formation of the cation radical originates from the triplet state. This hypothesis can explain the low radical quantum yield of D5-Zn^{II}Az48W because the efficiency of ISC is lower for D5-Zn^{II}Az48W than H5-Zn^{II}Az48W (as shown by the decreased phosphorescence intensity relative to fluorescence). It is important to note that the ability to generate triplet state is not the sole governing criteria for radical formation; the lower radical quantum yield for the ND-Zn^{II}Az48W isotopologue cannot be explained by the phosphorescence intensity. Both ND-Zn^{II}Az48W and H5-Zn^{II}Az48W have similar phosphorescence-fluorescence intensity ratios, indicating that the final radical quantum yield should also be similar in value based on the triplet-state hypothesis. However, this is not observed, and the lower Φ_{rad} of ND-Zn^{II}Az48W can, instead, be attributed to the proton transfer step of PCET.

Proton deprotonation and radical quantum yield. The proton transfer step can be slow in both D5-Zn^{II}Az48W• and Zn^{II}Az48W• formation. Although the N-H moiety of D5-Zn^{II}Az48W indole ring is not deuterated, the vibrational frequency of the W17 N-H bending mode is lower by 54 cm^{-1} in D5-Zn^{II}Az48W than the fully

protiated form because of contributions from the C-D bonds. This 54 cm^{-1} downshift in the W17 mode of closed shell D5-Zn^{II}Az48W is greater than the isotopic shift of 22 cm^{-1} observed for ND-Zn^{II}Az48W relative to the Zn^{II}Az48W. The W17 mode likely contributes to the deprotonation coordinate because it is reasonable to expect motions that involve the N-H bond to facilitate deprotonation. The different vibrational frequencies likely affect the deprotonation mechanism and proton transfer kinetics in D5-Zn^{II}Az48W and ND-Zn^{II}Az48W. Other trp vibrational modes that involve the N-H displacement (i.e. W17, W6, and W12 modes) can provide insights into the proton transfer event from the indole N-H moiety. Most of these vibrational modes are lower in frequency for D5-Zn^{II}Az48W and ND-Zn^{II}Az48W than for the fully protiated form, and these downshifts of the closed shell vibrational energies will affect the deprotonation event as well as the ET process (via the reorganization energy and electronic coupling between reactant and product[35]). However, these are hypotheses that need to be investigated with direct measurements of the rate of deprotonation and associated kinetic isotope effect (KIE). Upon H/D exchange of the indole N-H group, the ND-Zn^{II}Az48W derivative is hypothesized to have a slower rate of deprotonation, thus, a lower radical quantum yield based on the KIE.

The KIE is defined as the ratio of the rates of deprotonation of the protonated and deuterated (k_H/k_D) species. Here, we have not directly measured the rates of deprotonation but instead, focused on the rates of formation of the neutral species. We are assuming that the rates of formation of the neutral radical reflect deprotonation kinetics. The formation rates lead to the reported quantum yield for radical formation, and the ratio of these rates can be compared for NH-Zn^{II}Az48W and ND-Zn^{II}Az48W.

The resulting isotope effect, Φ_{rad} (NH-Zn^{II}Az48W)/Φ_{rad} (ND-Zn^{II}Az48W), is 1.47 (refer to quantum yield values of Table 3.2). The resulting value is greater than unity, indicating that deprotonation of the proton proceeds more efficiently than the heavier deuteron. This outcome suggests that the slower rate of formation of ND-Zn^{II}Az48W• is predominantly affected by the proton transfer pathway, as expected. The comparison of fluorescence and radical quantum yield values provides evidence that the rate-determining step is likely the final deprotonation of the cation radical (ND-Zn^{II}Az48W^{+}• or NH-Zn^{II}Az48W^{+}•) to form the neutral species, Zn^{II}Az48W•. In the case of the perdeuterated species, the rate-limiting step is not clear because both the fluorescence quantum yield and radical quantum yield of D5-Zn^{II}Az48W differ from the protiated form, indicating that changes are occurring in both the electron and proton transfer steps.

Besides the rate-limiting steps observed in trp-mediated PCET, the significance of the metal cofactor in forming neutral radical can be inferred from the photolysis of apo-Az48W. When the deuterated and protiated forms of Az48W are fully metallated with Zn(II), neutral radicals are observed upon photolysis of these holoprotein derivatives. However, with apoAz48W, the stable, neutral radical is not observed to buildup in the protein solution despite extended photolysis. Instead, a "transient" neutral radical can be seen only with continuous photolysis of UV light (based on results from Ignacio Lopez-Peña). The absence of an equilibrium buildup of the 515 nm band of the neutral radical during repeated photolysis of H5-apoAz48W is evident (Figure 3.6). However, the fluorescence and phosphorescence intensities are comparable to the protiated form of Zn^{II}Az48W. These observations suggest that the

absence of long-lasting, neutral radical may reflect changes in protein structure that do not stabilize the neutral radical. For example, if the empty metal pocket enables water to transiently enter the protein, the neutral radical may be overall unstable. Further experiments are needed to investigate the reasons for the different behavior of apo-Az48W relative to metalated forms of azurin.

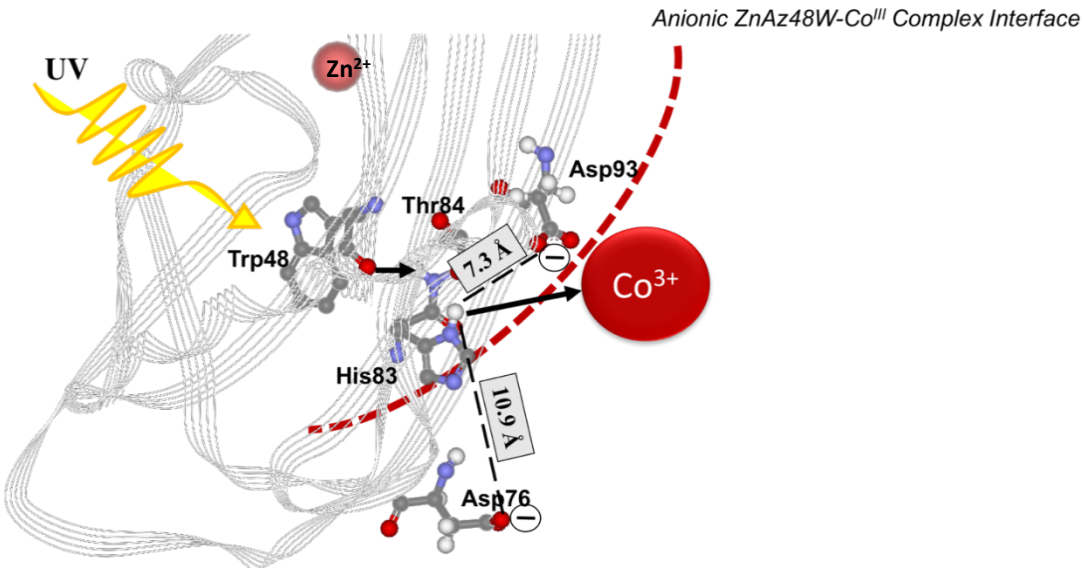

Figure 3.2: Proposed electron transfer mechanism of Zn^{II}Az48W to external Co^{III} acceptor in neutral pH buffer. Upon excitation with 228 nm UV light, the excited Trp-48 residue can donate its electron to the backbone of the nearby Thr-84 residue, where the electron tunnels through the hydrogen bond between carbonyl oxygen and the amino hydrogen. The electron tunnels through the backbone of Thr-84 to His-83, exiting to the nearest electron acceptor, Co^{III}. The Zn^{II}Az48W-Co^{III} anionic interface, in red dashed curve, displays the areas where Co^{III} can complex to the protein – in this case, it directly interacts with the negatively charged, acidic residues, Asp93 or Asp76. The electron can tunnel through the His-83 residue and travel the short distance to where Co^{III} is docked (at either sites of Asp-93 or Asp-76), reducing Co^{III} to Co^{II}. This proposed path is deduced from the crystal structure PDB 1e67.

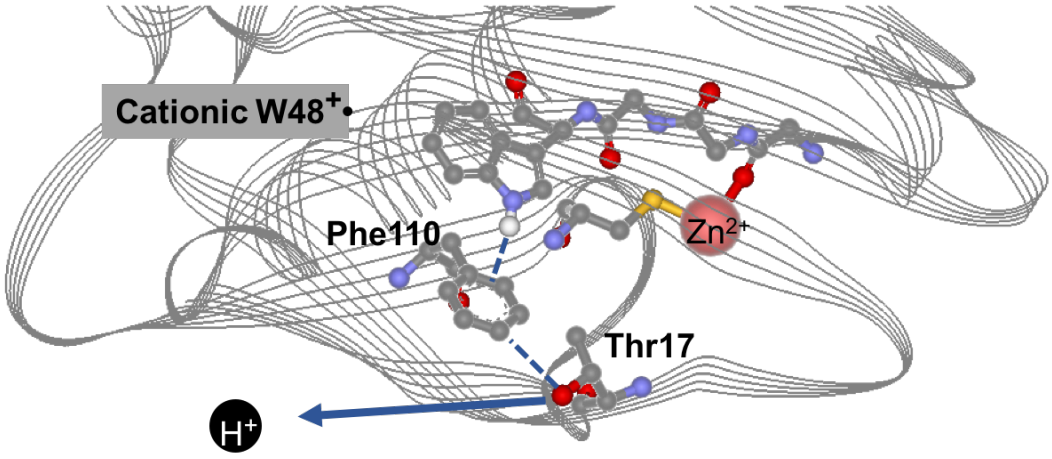

Figure 3.3: Proposed mechanism of proton transfer from the cation radical, Zn^{II} Az48W^{+}•, to generate neutral radical in neutral pH environment. The proposed mechanism of proton transfer is based off the crystal structure of wildtype Zn^{II}Azurin (PDB: 1e67). The proton from W48^{+}•, indicated in black, is able to tunnel through the pi-pi interactions between Trp-48 and Phe-110.

Table 3.1. Fluorescence quantum yields (Φ_{fluor}) and ratio of phosphorescence intensities to fluorescence for D5-Zn^{II}Az48W, ND-Zn^{II}Az48W, and fully protiated Zn^{II}Az48W, Cu^{II}Az48W and apo-Az48W.

Sample	**[a]Fluorescence Quantum Yield, Φ_{fluor}, in pH 7.2 Buffer**	**Fluorescence Quantum Yield, Φ_{fluor}, with Co^{III} Acceptor[d]**	**Phosphorescence Intensity Ratio in pH 7.2 Buffer Only[j]**	**Phosphorescence Intensity Ratio with Co^{III} Acceptor[i]**
D5-Zn^{II}Az48W	0.084[b]	0.11 ± 0.01[e]	0.0307	0.00457
ND-Zn^{II} Az48W	0.167 ±0.008	0.169 ± 0.009[f]	0.034 ± 0.006	0.00459
H5-Zn^{II}Az48W	0.19± 0.06[h]	0.20 ±0.07[g]	0.032 ±0.007	0.0052 ±0.0022
H5-Cu^{II}Az48W	0.0292± 0.0025	0.028 ±0.005	0	0
H5-apo Az48W	0.18[c]	-----	0.0362	-----

[a]Relative fluorescence quantum yields calculated with respect to known value of NATA in water (Φ_{fluor}= 0.13).
[b,c]The values are from a single experimental trial for D5-Az48W and apo-H5-Az48W.
[d]These samples have a 1:2 protein to Co(III) acceptor ratio, all in pH 7.2 phosphate buffer. [e,f]The error is derived from the uncertainty in the protein and Co^{III} concentrations after deoxygenating the system.
[g]The error is based on the number of trials for protiated H5NH-Zn^{II}Az48W with CoII acceptor (N=2).
[h]The error is calculated from all the trials for both the refolded H5NH- Zn^{II}Az48W (N=2) and that which did not undergo refolding conditions (N=2). [i,j]The phosphorescence intensity ratio is defined as $\lambda max, phos / \lambda max, fluor$, listed from one trial for all species except H5-Zn^{II}Az48W (N=3 and N=4, for with and without Co^{III}, respectively).

Table 3.2. Radical quantum yields (Φ_{rad}) of D5-Zn^{II}Az48W, ND-Zn^{II}Az48W, and fully protiated Zn^{II}Az48W. All samples are in pH 7.2 buffer and contain Co(III) acceptor in a protein:Co(III) ratio of 1:2.

SAMPLE TYPE	RADICAL QUANTUM YIELD, Φ_{RAD}
D5-Zn^{II}AZ48W	0.073[a]
ND-Zn^{II}AZ48W	0.086 ± 0.012[b]
H5-Zn^{II}AZ48W	0.127 ± 0.014[c]
APO- AZ48W	0

[a]The D5-Zn^{II}Az48W radical quantum yield is only based on one trial.
[b,c]The errors are reported as the standard deviation of the average value, where N=7 and N=5 for ND-Zn^{II}Az48W and H5-Zn^{II}Az48W, respectively.

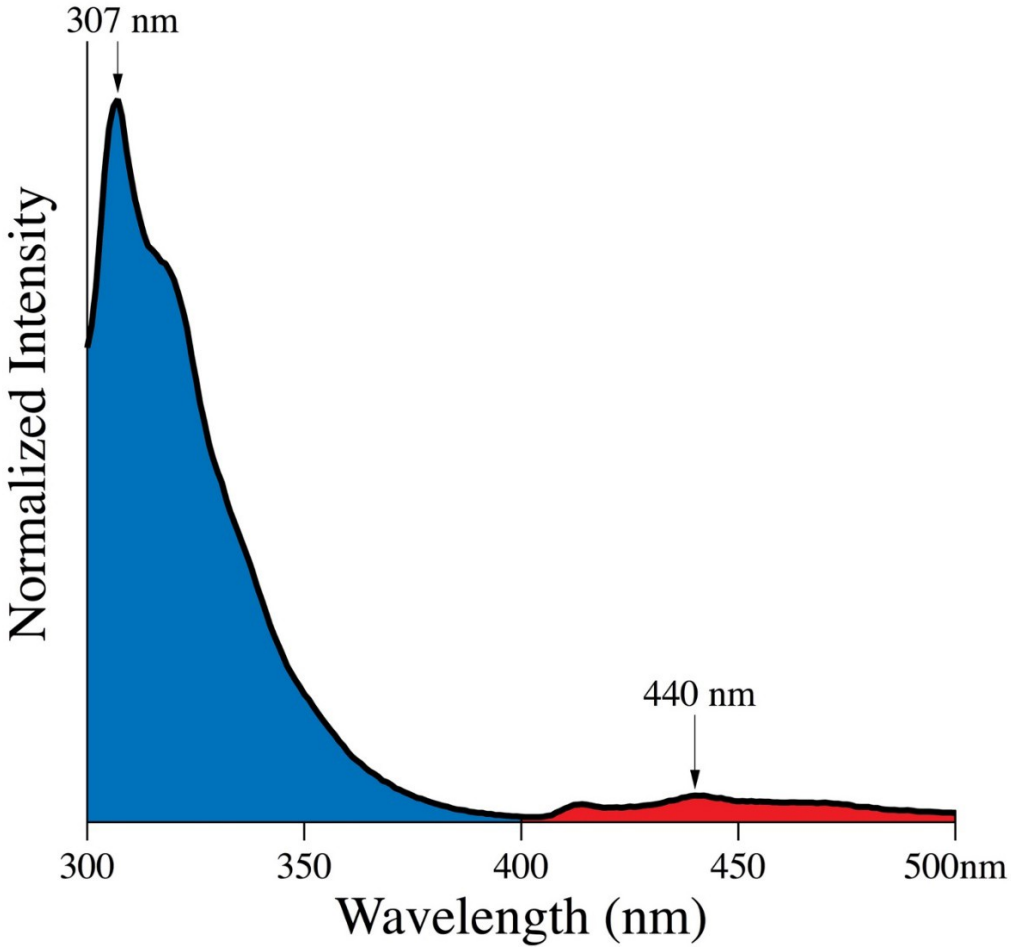

Figure 3.4: Representative emission spectrum of deoxygenated ND-Zn^{II}Az48W in pH 7.2 buffer, without Co^{III} electron acceptor. The fluorescence quantum yield, Φ_{fluor}, is reflected in the integrated area under the normalized fluorescence, ranging from 300 to 400 nm (colored blue). The phosphorescence emission ranges from 400 to 500 nm, as indicated in red. The peak intensities of the fluorescence and phosphorescence were taken at 307 nm and 440 nm, respectively, where the ratio of phosphorescence intensity is calculated as $I_{440nm} : I_{370nm}$.

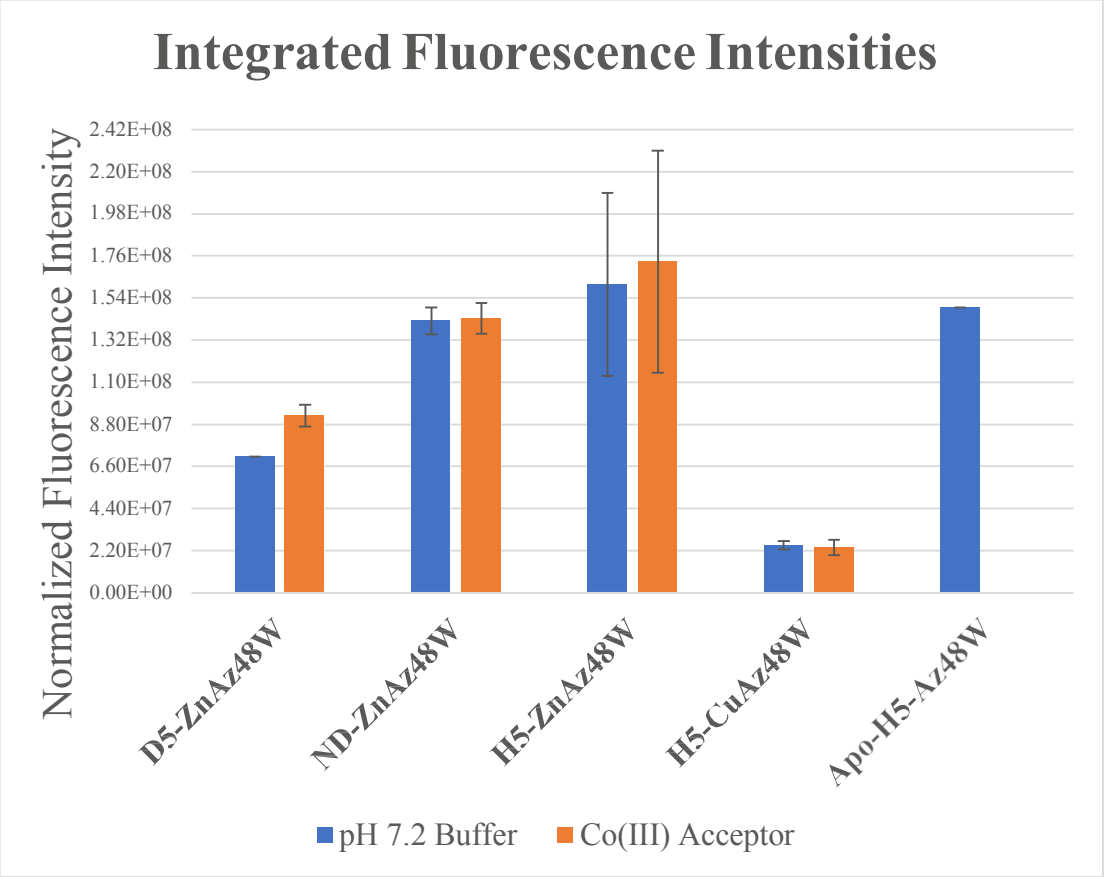

Figure 3.5: Summary of integrated fluorescence intensities of D5- Zn^{II}Az48W, ND-Zn^{II}Az48W, H5-Zn^{II}Az48W, Cu^{II}Az48W, and apo-H5-Az48W deoxygenated in pH 7.2 phosphate buffer, with and without Co^{III} acceptor. The normalized fluorescence intensity is taken by integrating the area under the fluorescence profile (from 300 to 400 nm) for each species, and normalizing with respective protein concentrations and water Raman band intensities. The water Raman intensity is taken in account to adjust for power fluctuations from the fluorometer. All samples are in pH 7.2 phosphate buffer, with or without Co^{III} acceptor. The designated error bars are derived from the number of trials for ND-Zn^{II}Az48W and H5-Zn^{II}Az48W in buffer only, which are N=2 and N=4, respectively. The error bars for D5-Zn^{II}Az48W and ND- Zn^{II}Az48W with CoIII acceptor are calculated from the corrected concentration of protein and acceptor after deoxygenating. The error for H5-Zn^{II}Az48W with Co^{III} is based off the number of trials (N=2). The error for Cu^{II}Az48W is based on the number of trials (N=4 for with and without Co^{III}), and the error for apo-Az48W is not reported because a single trial was performed.

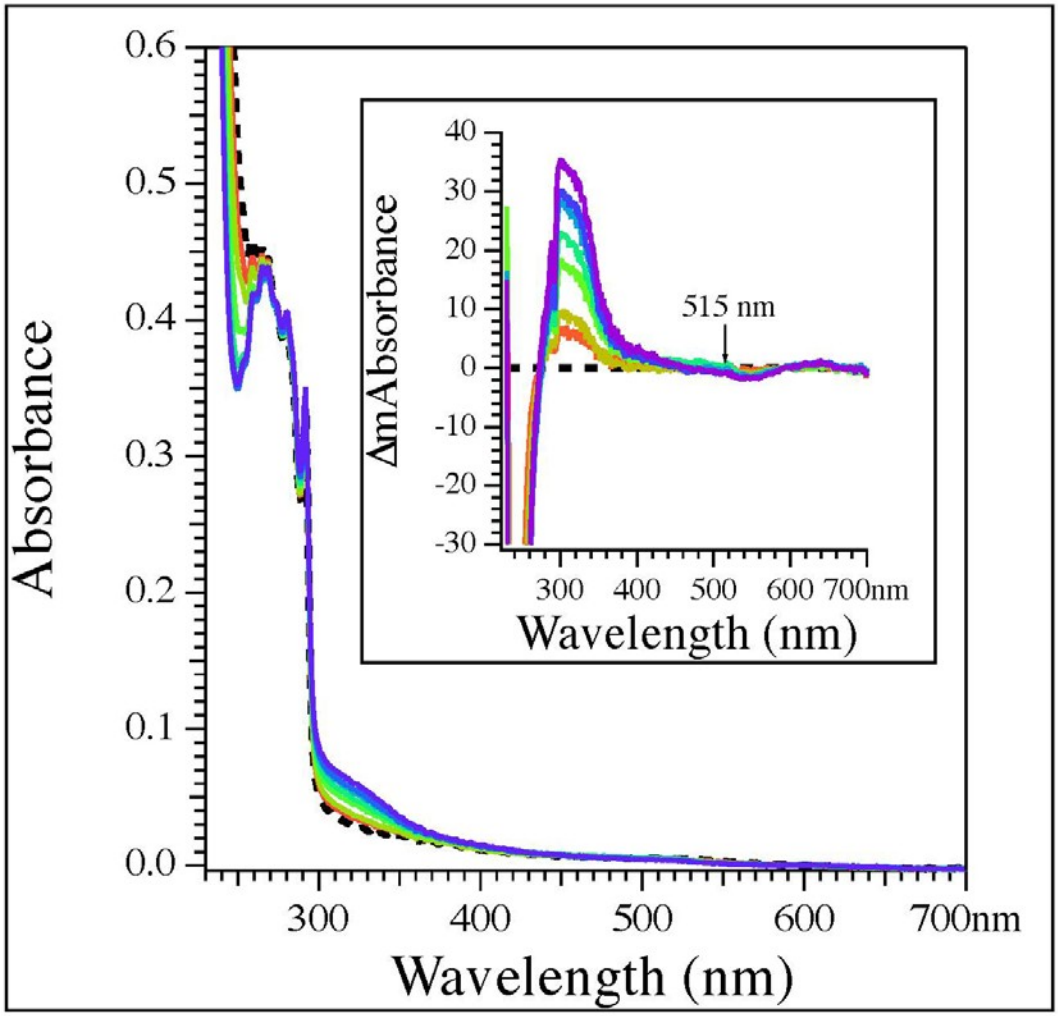

Figure 3.6: Photolysis (292 nm wavelength) of NH-apoAz48W with Co^{III} acceptor in 20mM phosphate buffer, pH 7.2. The different colored spectra were recorded after every 5-min interval, for a total of 30-min photolysis. An absorption at 515 nm of the neutral radical is nearly nonexistent. Any slight absorption may reflect contamination with holoprotein, Zn^{II}Az48W. The inset displays the difference spectra after subtracting the pre-photolysis absorption spectrum (dotted line) from the sequential post-photolysis spectra. The absorption at around 320 nm can be attributed to the presence of Co^{II}, reduced from Co^{III}, and protein photolysis byproduct.

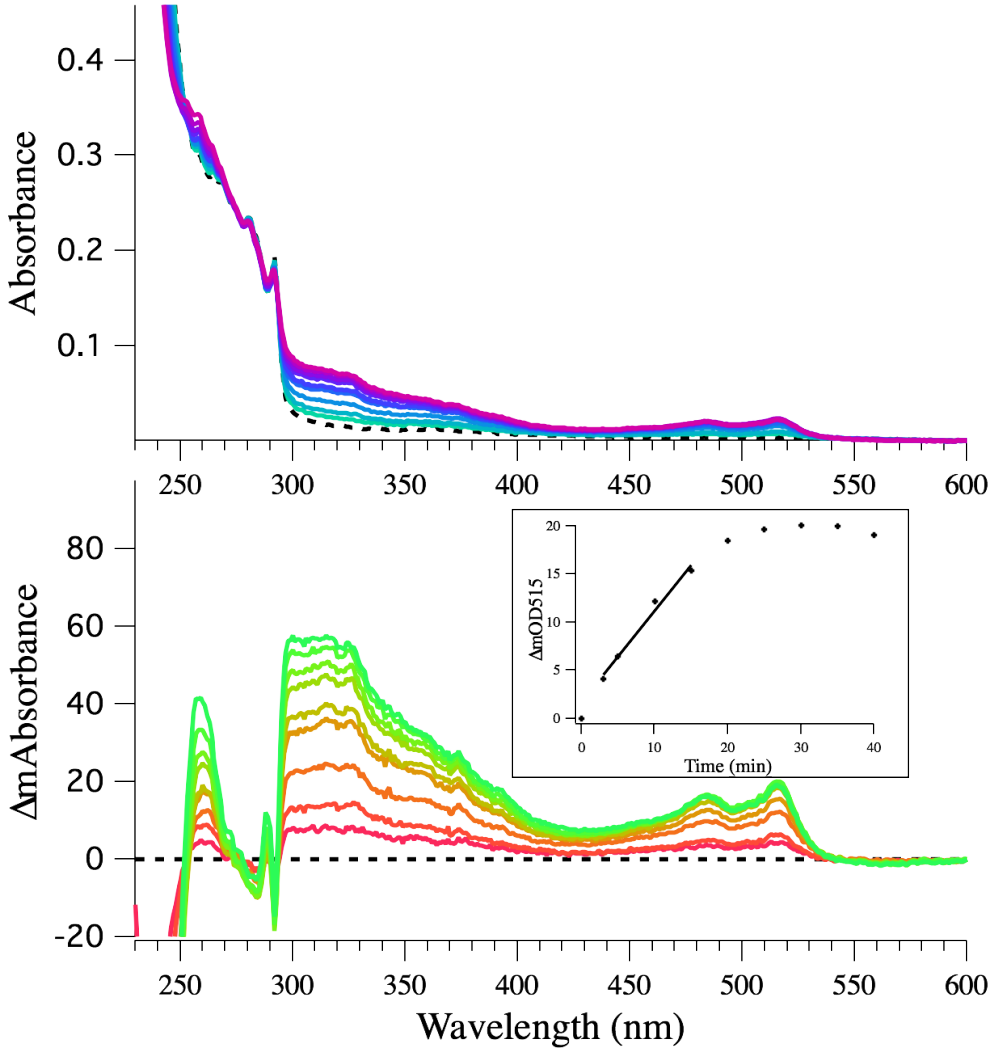

Figure 3.7: Absorption spectra of ND- Zn^{II}Az48W in pH 7.2 phosphate buffer and in the presence of Co^{III} acceptor. The total photolysis time is 40 minutes with 292 nm light. The top panel shows the absorption spectra of ND-Zn^{II}Az48W after subtraction of the baseline, and subtraction of the buffer spectrum. The bottom panel shows the difference spectra after subtracting the pre-photolysis spectrum (dotted line) from the post-photolysis spectra at each time point. The neutral radical peak absorption band grows in at 515 nm, as indicated. The inset displays ΔAbs at 515 nm over time (in minutes), where the radical yield rate is determined by the linear slope between 3 min and 15 min marks.

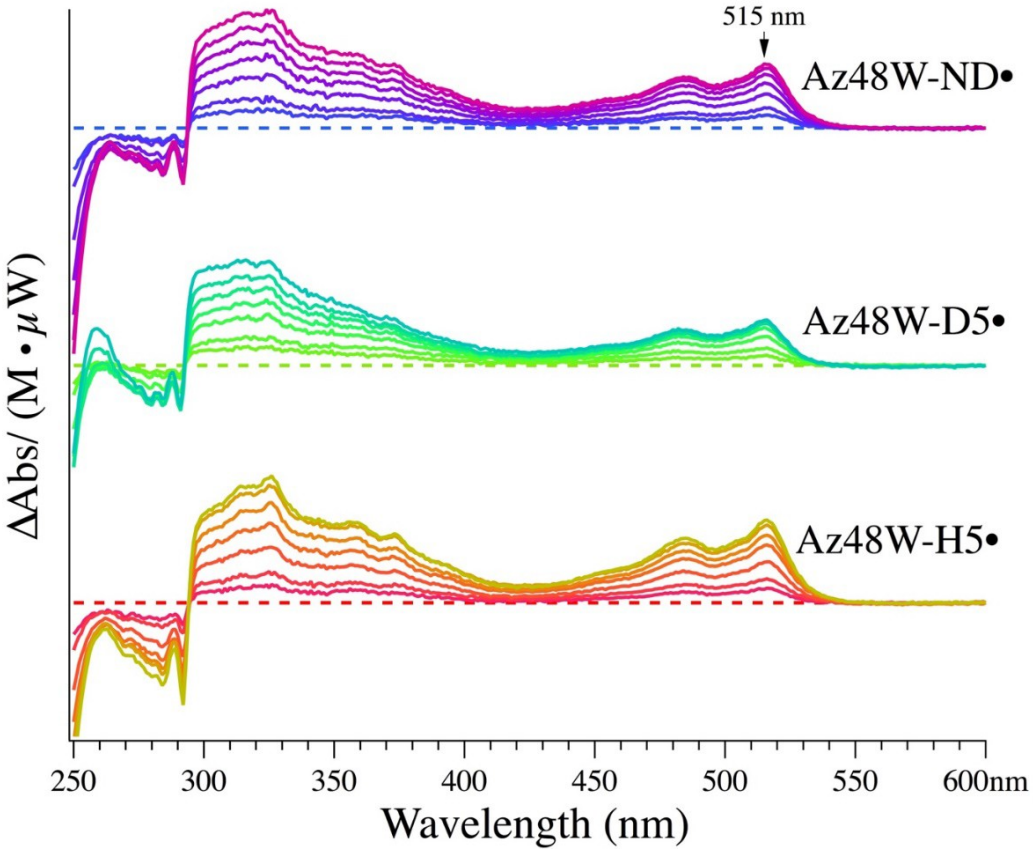

Figure 3.8: Normalized difference spectra of D5-Zn^{II}Az48W, ND-Zn^{II}Az48W, and NH-Zn^{II}Az48W in pH 7.2 phosphate buffer and in the presence of Co^{III} acceptor. Each spectrum displays spectra acquired at the 3-min mark and then at every 5-min interval of photolysis time. All difference spectra are normalized for protein concentration and photolysis power at 292 nm excitation. The dotted difference spectrum indicates the zero-minute mark, after subtracting the pre-photolysis spectrum from each post-photolysis spectrum.

4 Conclusion and Future Studies

4.1 Concluding Remarks

Electron transfer is modulated efficiently through amino acid mediators, where long-distant ET can be seen in several complex biological systems. In particular, tryptophan can facilitate electron transfer through a proton-coupled mechanism, where ET and PT occur in a stepwise fashion. Chapter 2 discussed the vibrational structures of the closed-shell and neutral radical of Az48W isotopologues. The second chapter focused on the mechanisms of electron and proton transfer of perdeuterated (D5-Zn^{II}Az48W) and singly-deuterated (ND-Zn^{II}Az48W) azurin derivatives.

The isotopic shifts apparent in the vibrational modes of D5-Zn^{II}Az48W and ND-Zn^{II}Az48W provide structural information of the embedded Trp-48 residue in Azurin. The observed frequency differences in the Trp normal modes upon isotopic exchange can provide insights into the electron and proton transfer process that results in the neutral radical formation. For instance, the lower vibrational frequency of the W17 mode may impact the deprotonation path, which can alter the yield for formation of the neutral radical. However, the mechanisms nor kinetics of ET and PT cannot be directly measured through the observation of Raman shifts. Instead, the fluorescence and radical quantum yields of isotopologues can provide some insights into the excited state of Zn^{II}Az48W and the deprotonation steps of $Az48W^{+}\bullet$, respectively. There appears to be a positive correlation between the phosphorescence intensities and radical yield noted for D5-Zn^{II}Az48W. However, an additional

consideration must be taken into account for ND-Zn^{II}Az48W because of the heavier mass of the deuteron. The isotopic effect, defined here as the ratio of the rate of neutral radical yield for Zn^{II}Az48W and ND-Zn^{II}Az48W, is greater than unity, suggesting that the deprotonation of this isotopologue is affected by the H/D exchange of the acidic proton on the indole ring.

4.2 Future Work

Besides fine-tuning the experimental values of fluorescence and radical yield in the azurin isotopologues (i.e. increasing the number of trials), additional methods and analyses should be performed to further define the electron transfer process in Az48W. Since the fluorescence quantum yield cannot absolutely define the excited state lifetime of Az48W, kinetic studies using transient absorption or emission should be pursued. Both time studies and spectral identification of the Trp-48 cation radical can be difficult to obtain, due to the rapid electronic transfer and deprotonation rates. These non-trivial studies are currently being pursued by a fellow Kim Group member, Joel Rivera.

As previously mentioned, it is hypothesized that the formation of cation radical is generated from the triplet state. The phosphorescence intensity can only provide a positive correlation in D5-Zn^{II}Az48W radical yield. Based solely on phosphorescence intensity, it cannot be completely ruled out that the singlet state does not contribute to radical generation. Therefore, further studies with the excitation of the triplet state can provide more insight into the

mechanism of cation and neutral radical formation. Ignacio Lopez-Peña, another member of the Kim Group, is currently studying the triplet state of Azurin.

Lastly, neutral radical is not observed when exciting the apoprotein form of Az48W. However, under constant illumination, the neutral radical absorption band is observed (reported by Ignacio Lopez-Peña). Therefore, the metal cofactor seems to play a significant role in allowing stable, neutral radical formation. Further experiments can be performed with Az48W metallated with metals other than Zn(II), in order to confirm the importance metal cofactor on redox protein function.

REFERENCES

1. Gray, H.B.; Winkler, J.R. Long-range electron transfer. *Proc.Natl.Acad.Sci.* **2005**; 102: 3534 – 3539.

2. Westerlund, K. Berry, B.W., Privett, H.K., Tommos, C. Exploring amino-acid radical chemistry: protein engineering and de novo design. *Biochim.Biophys.Acta.* **2005**; 1707: 103 – 116.

3. Eklund, H.; Uhlin, U.; Farnegardh, M.; Logan, D.T.; Nordlund, P. Structure and function of the radical enzyme ribonucleotide reductase. **2001**; 77: 177-268.

4. Faller, P., Debus, R.J.; Brettel, K.; Sugiura, M.; Rutherford, A.W.; Boussac, A. Rapid formation of the stable tyrosyl radical in photosystem II. *P.Natl.Acad.Sci.USA*. **2001**, 98: 14368 – 14373.

5. Reece, S.Y., Nocera, Daniel G., Proton-Coupled Electron Transfer in Biology: Results from Synergistic studies in Natural and model Systems. *Annu. Rev. Biochem*. **2009**; *78*: 673 – 699.

6. Sancar, A. Structure and Function of DNA Photolyase and Cryptochrome Blue-Light Photoreceptors. *Chem.Rev.* **2003**; 103: 2203 – 2237.

7. Lukacs, A.; Eker, A.P.; Byrdin, M.; Villette, S.; Pan, J.; Brettel, K.; Vos, M.H. Role of the middle residue in the triple tryptophan electron transfer chain of DNA photolyase: ultrafast spectroscopy of a Trp →Phe mutant. *J.Phys.Chem.B.* **2006**; 110: 15654 – 15658.

8. Vijgenboom, E. ; Busch, J.E.; Canters, G.W. *In vivo* studies disprove an obligatory role of azurin in denitrification in *Pseudomonas aeruginosa* and show that *azu* expression is under control of RpoS and ANR. *Microbiology*. **1997**; *143*: 2853-2863.

9. Larson, B.C.; Pomponio, J.R.; Shafaat, H.S.; Kim, R.H.; Leigh, B.S.; Tauber, M.J.; Kim, J.E. Photogeneration and Quenching of Tryptophan Radical in Azurin. *J.Phys.Chem.B.* **2015;** 119: 9438 – 9449.

10. Shafaat, H.S.; Leigh, B.S.; Tauber, M.J.; Kim, J.E. Spectroscopic Comparison of Photogenerated Tryptophan Radicals in Azurin: Effects of Local Environment and Structure. *J.Am.Chem.Soc.* **2010**; *132*: 9030 – 9039.

11. Cleland, W.W. The Use of Isotope Effects to Determine Enzyme Mechanisms. *J.BiolChem.* **2003**; *278*: 51975 – 51984.

12. Edwards, S.; Soudackov, A.V., Hammes-Schiffer, S. Analysis of Kinetic Isotope Effects for Proton-Coupled Electron Transfer Reactions. *J.Phys.Chem.A.* **2009**; 113: 2117 – 2126.

13. Miller, J. E.; Gradinaru, C.; Crane, B. R.; Di Bilio, A. J.; Wehbi, W. A.; Un, S.; Winkler, J. R.; Gray, H. B. Spectroscopy and reactivity of a photogenerated tryptophan radical in a structurally defined protein environment. *J. Am. Chem. Soc*. **2003**; 125:14220−14221.

14. Di Bilio, A. J.; Crane, B. R.; Wehbi, W. A.; Kiser, C. N.; Abu-Omar, M. M.; Carlos, R. M.; Richards, J. H.; Winkler, J. R.; Gray, H. B. Properties of photogenerated tryptophan and tyrosyl radicals in structurally characterized proteins containing rhenium(I) tricarbonyl diimines. *J. Am. Chem. Soc*. **2001**; 123: 3181−3182.

15. Larson, B.C. (2013). Modulation of proton-coupled transfer electrons in azurin: quantum yield and pKa analyses. (Master of Science Thesis). University of California, San Diego.

16. Lancaster, K.M.; Farver, O.; Wherland, S.; Crane, E.J., 3rd; Richards, J.H.; Pecht, I.; Gray, H.B. Electron transfer reactivity of type zero Pseudomonas aeruginosa azurin. *J.Am.Chem.Soc.* **2011**; 133: 4865 – 4873.

17. Nar, H. Huber, R., Messerschmidt, A. Filippou, A.C., Barth, M., Jaquinod, M., van de Kamp, M., Canters, G.W. Characterization and crystal structure of zinc azurin, a by-product of heterologous expression in Escherichia coli of Pseudomonas aeruginosa copper azurin. **1992**; 2015: 1123-1129.

18. López-Peña I, Leigh BS, Schlamadinger DE, Kim JE. Insights into Protein Structure and Dynamics by Ultraviolet and Visible Resonance Raman Spectroscopy. *Biochemistry*. **2015**;54:4770-4783.

19. Schlamadinger, D.E.; Gable, J.E.; Kim, J.E. Hydrogen Bonding and Solvent Polarity Markers in the UV Resonance Raman Spectrum of Tryptophan: Application to Membrane Proteins. *J. Phys. Chem. B*. **2009**; *113*: 14769–14778.

20. Sanchez, K.M.; Neary, T.J.; Kim, J.E. Ultraviolet resonance Raman spectroscopy of folded and unfolded states of an integral membrane protein. *J.Phys.Chem.B.* **2008**; 112: 9507 – 9511.

21. Harada, I.; Takeuchi, H. Raman and Ultraviolet Resonance Raman Spectra of Proteins and Related Compounds. *Spectroscopy of Biological Systems*. **1986.**

22. Frisch, M.J.T. *GaussView*; Gaussian, Inc.: Wallingford, CT, 2004.

23. ChemCraft URL citation: https://www.chemcraftprog.com

24. Grafton, A.K. 'Vibalizer: A free, Web-Based Tool for Rapid, Quantitative Comparison and Analysis of Calculated Vibrational Modes' J. Comput. Chem. 2007, v 28, pp 1290-1305.

25. Shafaat, H.S.; Leigh, B.S.; Tauber, M.J.; Kim, J.E. Spectroscopic Comparison of Photogenerated Tryptophan Radicals in Azurin: Effects of Local Environment and Structure. *J.Am.Chem.Soc.* **2010**; Supplemental Materials (Table S3).

26. Dieng, S.D.; Schelvis, J.P.M. Analysis of Measured and Calculated Raman Spectra of Indole, 3-Methylindole, and Tryptophan on the Basis of Observed and Predicted Isotope Shifts. *J.Phys.Chem*. **2010**; 114: 10897 – 10905.

27. Lakowicz, J.R. Principles of Fluorescence Spectroscopy, 3re edition. **2006**.

28. Matthews,H.R.; Matthews, K.S.; Opella, S.J. Selectively deuterated amino acid analogues. Synthesis, incorporation into proteins and NMR properties. *Biochim.Biophys.Acta*. **1977**; 497:1-13.

29. Leckner, J.; Bonander, N.; Wittung-Stafsheded, Pernilla; Malmström, B.G.; Karlsson, B.G. The effect of the metal ion on the folding energetics of azurin: a comparison of the native, zinc and apoprotein. *Biochim.Biophys.Acta*. **1997**.1342:19-27.

30. Hansen, J.E.; McBrayer, M.K; Robbins, M.; Suh, Y. A pH dependence study on the unfolding and refolding of apoazurin: comparison with Zn(II) azurin. *Cell. Biochem.Biophys*. **2002**. 36: 19 – 40.

31. Wilson, C.J.; Apiyo, D.; Wittung-Stafshede, P. Solvation of the folding-transition state in *Pseudomonas aeruginosa* azurin is modulated by metal. *Protein.Sci*. **2006**.15: 843–852.

32. Nar, H.; Messerschmidt, A.; Huber, R.; van de Kamp, M.; Canters, G.W. Crystal structure of Pseudomonas aeruginosa apo-azurin at 1.85 A resolution. *FEBS.Lett*. **1992**; 306: 119 – 124.

33. Muiño, P.L.; Callis, P.R. Solvent Effects on the Fluorescence Quenching of Tryptophan by Amides via Electron Transfer. Experimental and Computational Studies. *J.Phys.Chem.B*. **2009**; 113: 2572 – 2577.

34. Montalti, M.; Credi, A.; Prodi, L.; Gandolfi, M.T. Handbook of Photochemistry, 3rd edition. *Taylor and Francis Group ILC*. **2006**.

35. Stubbe, J.; Nocera, D.G.; Yee, C.S.; Chang, M.C.Y. Radical Initiation in the Class I Ribonucleotide Reductase: Long-Range Proton-Coupled Electron Transfer? *Chem.Rev.* **2003**; 103: 2167 – 2202.

36. Petrich, J.W.; Longworth, J.W.; Fleming, G.R.; Internal Motion and Electron Transfer in Proteins: A Picosecond Fluorescence Study of Three Homologous Azurins. *Biochemistry*. **1987**; 26: 2711 – 2722.

37. Strambini, G.B., Gabellieri, E. Phosphorescence from Trp-48 in Azurin: Influence of Cu(II), Cu(I), Ag(I), and Cd(II) at the Coordination Site. *J.Phys.Chem.* **1991**; 95: 4352 – 4356.